Evidence of recent plutonic magmatism beneath Northeast Peloponnesus (Greece) and its relationship to regional tectonics

Tzanis, A.[1], Efstathiou, A.[1], Chailas, S.[1] and Stamatakis, M.[2]

[1] Section of Geophysics – Geothermy, National and Kapodestrian University of Athens, Panepistimiopoli, Zografou 15784, Greece.

[2] Section of Economic Geology and Geochemistry; National and Kapodestrian University of Athens, Panepistimiopoli, Zografou 15784, Greece.

Corresponding Author: Andreas Tzanis, atzanis@geol.uoa.gr

Reference: Tzanis, A., Efstathiou, A., Chailas, S. and Stamatakis, M., 2018. Evidence of recent plutonic magmatism beneath Northeast Peloponnesus, Greece, and its relationship to regional tectonics, *Geophys. J. Int.*, 212, 1600-1626, doi: 10.1093/gji/ggx486.

Athens, August 2017

ABSTRACT

The present work reports evidence of recent tectonically controlled plutonic magmatism related to Neogene volcanism in a broad area of Northeast Peloponnesus (Greece) that is straddled by the Hellenic Volcanic Arc (HVA) and comprises the Argolid, the Argolic and Saronic gulfs and eastern Corinthia including the province of Crommyonia at the western half of Megaris peninsula (western Attica). We assess the contemporary stress field based on formal inversion of well-constrained crustal earthquake focal mechanisms and determine that it is principally extensional and NE-SW oriented, with σ_1 strike and plunge being N64° and 77° respectively and σ_3 strikes and plunge N210° and 10°. This generates WNW-ESE and NW-SE faults, the former being dominant in the Saronic Gulf and the latter in the Argolic. In addition, the analysis predicts E-W and N330° faults with non-trivial right-lateral and left-lateral heave respectively, which are consistent with the R and R′ directions of Riedel shear theory and explain a number of observed earthquake focal mechanisms and earthquake epicentre alignments. We also present a semi-quantitative analysis of observed aeromagnetic anomalies by performing numerical modelling of the radially averaged power spectrum with an efficient anomaly separation scheme based on a new type of 2-D Fourier domain filter introduced herein, the Radial Extended Meyer Window. This analysis identifies an extensive complex of magnetized rock formations buried at depths greater than 3km which, given the geology and geotectonic setting of the area, can hardly be explained with anything other than calc-alkaline intrusions (plutons). At north-eastern Corinthia and Crommyonia, this type of intrusive activity is unexceptional, mainly concentrated in the Gulf of Megara – Sousaki areas and consistent with the low-intensity, small-scale Pliocene dacitic volcanism observed therein. Conversely, large-scale elongate anomalies of E-W and N330° orientation have been identified in the Argolid, generally collocated with and delimited by extensional tectonic structures (grabens and major faults) of analogous orientation. These are interpreted to comprise calc-alkaline plutons whose placement has been controlled by the regional tectonic activity (syn-rift magmatism); their nature and origin is demonstrated with convergent evidence from deep magnetotelluric, seismological, seismic tomography and other investigations. A large number of shallow and superficial (less than 2km) magnetic sources have also been identified; these are generated by a complex of distributed near-surface formations consisting of sub-vertically developing buried or extrusive volcanics and outcropping or shallow-buried ophiolitic formations (thin nappes of tectonic mélange and dismembered ophiolitic complexes). The joint analysis of the data facilitates the formulation of a tentative geotectonic model for Argolis peninsula, according to which the strain differential caused by the disparate extensional trends of the Argolic and Saronic gulfs is accommodated by right-lateral block motion associated with igneous intrusive activity at major block boundaries.

1. Introduction

The area of NE Peloponnesus (Argolid and Corinthia) is not only geologically complex but is also part of a fascinating contemporary geotectonic setting (Fig. 1). As will be reviewed in Section 2, it is part of the broader Corinth Rift (CR) system and is bounded by the W-E oriented Gulf of Corinth (GoC) to the north, which is the rapidly spreading core of CR, by the NW-SE oriented extensional subsystem (graben) of the Argolic Gulf and Argolic Plain to the west and by the complex extensional structures of the Saronic Gulf to the east. In addition, it is underlain by the Hellenic Subduction System whose local geometry and influence on crustal tectonics is certainly not simple and as yet imprecisely understood. As part of this system, the Peloponnesian Northeast is straddled by the NW-SE oriented Hellenic Volcanic Arc –also known as South Aegean Volcanic Arc– and features two known volcanic fields: the small Methana Volcanic Complex at the east coast of the Argolid and the local-scale Sousaki solfatara at Crommyonia, near the southern margin of the GoC (Fig. 1 and 2). However, with the exception of these fields, the broader CR area appears to not exhibit some type of syn-rift volcanism, a characteristic also unique among other active rift systems.

In spite of the interest it apparently presents as part of a very active roll-back system with active volcanism, and by all probability due to its low seismicity rate, the Peloponnesian Northeast has rarely been the focus of specialized or trans-disciplinary research and has undeservingly not attracted as much attention as that directed to the GoC area. The pre-Alpine geology and tectonics are rather more extensively studied than their post-Alpine counterparts and contemporary crustal deformation has not been examined to an appreciable level. GPS surveys have been limited to the GoC. All but one published examples of seismological work have focused on deep structures and processes and the sole crustal seismicity study was confined to the Saronic Gulf and did not address questions about the configuration of the stress field and associated deformation modes. The primary coastal and offshore neotectonic extensional faulting structures are rather successfully mapped by marine geophysical surveys in the Argolic and Saronic gulfs but little is actually known of the secondary and auxiliary onshore and offshore faulting modes, let alone of their causative stress field. Onshore geophysical work focusing on large or regional scale crustal structures has not been carried out; the possibility of past or present syn-rift magmatic activity is undetermined.

In this study we focus on a rather broad area straddled by the northwest branch of the HVA, which includes the Argolid, the Argolic and Saronic gulfs and eastern Corinthia including the area of Crommyonia at the west of Megaris peninsula, where the Sousaki solfatara is located (Fig. 1 and Fig. 2). We address questions relating to the configuration of the crustal stress field and deformation modes, as well as to the existence of (syn-rift) magmatism and its relationship to crustal deformation. To this effect, we use all available earthquake focal mechanisms and formal stress inversion in order to deduce the contemporary stress field, constrain the resulting active faulting modes and correlate them with geologically mapped faults and fault zones. We also use a well-constrained aeromagnetic data set together with an efficient magnetic anomaly separation scheme, in order to distinguish between the magnetic signatures of deep-seated and shallow-buried or superficial rock formations. Given the geotectonic setting of the area, deep-seated formations can hardly be explained with anything other than calc-alkaline intrusions (plutons). To this end, we use deep magnetotelluric, seismological, seismic tomography and other information to argue for the origin and nature of the intrusions. With these lines of evidence it may be possible to make some progress in deducing the

existence of syn-rift magmatism by correlating the geometry and location of deep-seated magnetized rocks with respect to the active extensional and transtensional faulting structures.

2. Tectonics and Geology

Section 2 provides a thorough review of the complex geodynamic tectonic and geological setting of our study area and comprises four parts. Sections 2.1 and 2.2 respectively comprise an exposé of the large scale dynamics responsible for the Quaternary – Holocene calc-alkaline crustal magmatism and the tectonic framework facilitating the emplacement of these magmas. Additionally to providing geological context, this information is essential for the interpretation of the deep aeromagnetic anomaly sources. Observable magnetic anomalies can also be generated by mostly near-surface Mesozoic ophiolitic tectonic mélange, emplaced by alpine thin-skinned tectonics and further deformed by neotectonic activity**.** A large part of the work presented herein aims at separating the magnetic signatures of these profoundly different suites of rock. To this end, Section 2.3 provides an overview of the Quaternary volcanism and Section 2.4 a review of the geology and magnetic properties of the ophiolitic formations. This information is essential in understanding the context of the near-surface anomaly sources and interpreting the results of the separation exercise.

2.1 Geodynamic Setting

A defining deep dynamic feature with profound influence on crustal tectonics, as well as genitor of the Hellenic Volcanic Arc (HVA), is the active subduction of the African oceanic crust beneath the Aegean plate Hellenic Subduction System (HSS). The HSS exhibits changes in the rate and direction of subduction along its length (Fig. 1). At present, rapid subduction occurs along an arcuate belt of approximately 400 km between the islands of Crete to the south and Kefallinia to the NW; the front of the subduction is clearly defined by the bathymetry of the Hellenic Trench and the rate of convergence is estimated at 40 mm/yr (Clarke et al. 1998; McClusky et al. 2000).

In the vicinity of the study area, the subducting slab is NNW oriented and plunges to the E-NE. The geometry and internal structure of the slab are not uniquely determined and the isodepth contours shown in Fig. 1 are only based on one interpretation of the available data, (Basili et al., 2013). Specifically, the subduction is associated with a Wadati–Benioff zone which, according to Papazachos et al. (2000), is dipping at approx. 30° from 20 to 100 km depth and at approx. 45° from 100 to 150 km. These authors locate the 100 km iso-depth, hence the inflection of the slab, beneath an imaginary line passing through Hermionis and the Isthmus of Corinth, which is offset by approx. 25 km to the west of the 100km iso-depth depicted in Fig. 1. By mapping hypocentres and focal plane mechanisms of sub-crustal earthquakes, Hatzfeld et al. (1989) place the inflection at a depth of 50–60 km, at a zone consistent with the geographical location and orientation of the Argolic Gulf; they also place the 100km iso-depth at a zone consistent with the geographical location of the HVA and Methana Volcanic Complex (MVC) at the NE coast of the Argolid. This is compatible with the depths at which eclogite facies metamorphism drives water into the mantle wedge and initiates the generation of andesitic magmas and arc volcanism (e.g. Grove et al., 2006 and references therein). No inflection is detected in the 2-D tomographic analysis of Suckale et al., (2006) who image a rather thin (~10km) slab plunging at 21° to a depth of approx. 90 km beneath the Crommyonian volcanic field (see Fig. 1 and Fig. 2). This is not consistent with earthquake activity at depths greater than 100 km beneath the

Saronic Gulf and Attica (see Section 5 for details). It is also not consistent with the tomographic imaging of Sachpazi et al. (2016), who identify an inflection at approx. 60km beneath the Argolic Plain (Fig. 2). These authors also detect segmentation in the slab, caused by along-dip faults in a manner suggestive of mechanical coupling with the overriding (Aegean) plate that strongly influences the deformation of the latter.

The thickness of the upper (overriding) plate is a factor significantly influencing the manifestation and type of crustal magmatism; it is also not uniquely determined in our study area. For example, Drakatos et al (2005) assert that it is limited to about 20 km and attribute their observation to the extensional thinning and the emergence of the mantle material which, they assert, reaches up to the depth of 12 km consistently with the estimation of the depth to the Curie isotherm given by Tselentis (1991). On the other hand, Sachpazi et al. (2007), Suckale et al., (2009) and others, place the upper (Aegean) plate Moho at approx. 37 km beneath the west coast of the Argolic Gulf and 30km beneath the western Saronic. This indicates significant thinning of the Aegean crust between east Peloponnesus and the Saronic Gulf, initiating approximately beneath the Argolic Gulf and Plain. The deep magnetotelluric study of Galanopoulos et al. (2005) detects a "wall" of relatively conductive material beneath an onshore location a few kilometres north of the head of the Argolic Gulf, which appears to transgress the base of the Aegean plate crust and spread sideways beneath the Peloponnesus. As will be argued in Section 5, this points to partial melting in the upper mantle and subducting crust and may be related to the inflection of the slab and the thinning of the Aegean plate crust. All the above evidence indicate that the inception and evolution of the Argolic Gulf may be related to deep-rooted processes and may comprise a major component of the geotectonic setting of the study area. Analogous and significantly broader columns of conductive material appear to upwell from the subducting slab at a depth of approx. 100km and rise through the mantle wedge to the base of the crust beneath Crommyonia: this is direct manifestation of partial melting associated with the HVA.

2.2 Regional Tectonics

In the Aegean plate, the area between the dextral Kefallinia Transform (Fig. 1) and the Aegean Sea defines the Central Hellenic Shear Zone (CHSZ) of trans-tensional deformation, with displacement rates of the order of 25 mm/year (Peter et al. 1998; Kahle et al., 2000). Within this zone of active extension lies the rapidly spreading Corinth Rift (CR): this is a young W-E oriented extensional graben developing in a compressional regime of continental collision and manifesting high complexity and increased seismicity and deformation rates: a NNW-SSE oriented extensional stress field generates W-E normal faults and accommodates the strain produced by the dextral shear motions of North Anatolian/ North Aegean fault systems to the E-NE and the Kefallinia Transform to the west. The most active contemporary feature of the CR is the W-E oriented Gulf of Corinth (GoC), described as a composite asymmetric graben (Stefatos et al., 2002) with varying geometry along strike (Sachpazi et al., 2003; McNeill et al., 2005). Extensive geological studies of the GoC fault system (e.g. Doutsos and Piper, 1990; De Martini et al., 2004; Flotté et al. 2005; McNeil et al. 2005), earthquake focal mechanisms (e.g. Rigo et al., 1996) and geodetic investigations (e.g. Billiris et al., 1991; Briole et al., 2000; Avallone et al., 2004), have shown that the GoC is subjected to N-S extension of 1.0 – 1.6 cm/yr, with higher rates observed at the west and lower rates at the centre of the rift. Armijo et al. (1996) suggest that 50-75% of the total extension rate (~0.7 cm/yr) is accommodated through high-angle normal faulting, although this may be an overestimation (Westaway, 2002). The W-E active faults of the CR appear to extend eastwards in a diffuse zone through central Greece (e.g. Goldsworthy

and Jackson, 2001). Skourtsos and Kranis (2009) have found extensional structures with geometrical and kinematic characteristics analogous to those of known GoC faults as far south as the northern flanks of Mt Mainalon, (approx. 37.7°N), about 30 km to the west of our study area. It is also possible that the evolution of the CR is decorated with episodic-type accelerated deformation events, presumably associated with deep-seated interactions between the southward-moving Aegean continental forearc and the subducting African oceanic plate (Leeder et al., 2012).

The areas of the Argolid and the Argolic and Saronic Gulfs are closely related to the Corinth Rift system. However, contrary to the exhaustively investigated Gulf of Corinth (GoC), these areas have not been as thoroughly studied. The Argolis Peninsula is flanked by the Argolic Gulf to the west and the Saronic Gulf to the east (Fig. 2). According to Papanikolaou et al. (1988), the Argolic Gulf is a symmetric basin of NW-SE orientation and during the Pliocene – Early Pleistocene formed a channel joining the south Aegean Sea with the GoC and isolating the peninsula from the rest of the Peloponnese. The main faults there have NW-SE and rarely ENE-WSW orientation. Van Andel et al. (1993) characterize the Argolic Gulf as a half-graben, in which the eastern marginal faults are a brittle response to downwarping. They also assert that it is an active structure with Holocene subsidence rates along its western margin increasing from about 50 cm/ka near Argos to 100 cm/ka near the mouth of the Gulf, and along its eastern margin from zero near Nafplion to 150 cm/ka in the vicinity of Spetsai Island. Seismological evidence by Drakatos et al. (2005) indicate that the Saronic Gulf is divided in two basins by a central platform which, they conjecture, is the offshore extension of a large thrust belt dominating the adjacent onshore areas of Attica. The western basin is characterized by higher seismic activity and is furthermore distinguished into a northern and a southern block by a seismologically well-defined W-E rupture zone which is located between Aegina and Salamis islands, extends onshore into the Peloponnese and is interpreted to comprise an extension of the Corinth Rift faulting system.

A line of evidence suggests that the expression of normal faulting changes from W-E at the Gulf of Corinth to WNW-ESE in Saronic (approx. N110° on average, Papanikolaou et al., 1988) and to NW-SE at the Cyclades (S. Aegean) in two discrete steps (e.g. Papanikolaou and Lozios, 1990). This indicates a corresponding rotation of the σ_3 principal stress axis. Based on their analysis of the surrounding areas and a single focal mechanism of the Mw = 5.2 event of 4/7/1968 by Ritsema (1974), Kiratzi and Louvari (2003) suggest that in the Saronic, the extensional field has NNE-SSW orientation. Their conclusion is corroborated by four mechanisms of small crustal earthquakes located at the Argolid and published by Hatzfeld et al. (1993).

Whereas the main deformation mode in the Argolic and Saronic gulfs appears to be NW-SE extension, such faults can only be observed at the NE and SW coasts of Argolis peninsula, corresponding to the NE dipping boundary faults of the Saronic and the SW dipping boundary faults of the Argolic gulfs. As summarized in Vassilopoulou (1999, 2010; references therein), within the peninsula the main orientation of major terrain features and morphological discontinuities is W-E and the orientation of neotectonic faulting structures and zones is mainly WNW- ESE to W-E. These structures form a series of local horsts and grabens with particular reference to the Mt Adheres area at the SE and Hermionis peninsula at the SW; they are most active at the south and SE, where they contribute to the formation of the tectonic basin of Hydra Gulf and Strait, as well as at the SW, towards Kranidi and the Argolic Gulf (Fig. 2).

2.3 Quaternary Volcanism

Quaternary to contemporary volcanism is manifest in the Methana Volcanic Complex (MVC) which is located at the NE coast of Argolis Peninsula, as well as in the Sousaki solfatara field located at the Crommyonia province of north-eastern Corinthia (terminus of the Hellenic Volcanic Arc). The Sousaki solfatara, (e.g. Francalanci et al., 2005 and reference therein), is the relic of a small volcanic field that used to be active between 4 and 2.3 Ma (Late Pliocene – Early Quaternary). The observable volcanic outcrops are generally small (total volume less than 1 km^3); they are distributed over a large area and consist of dacitic lava domes and associated lava flows. Vent distribution and edifice shapes exhibit W-E and NW-SE anisotropy and appear to be controlled by tectonic lineaments of analogous orientation, related to the Corinth Rift system. Explosive activity concurrent with the emplacement of lava domes is evident by layers of tuffs and tuffites found in lacustrine deposits of the same age as the volcanic outcrops. The Sousaki area today hosts a low-temperature geothermal field (up to 80°C) and weak fumarolic activity emitting low temperature gasses (30-40°C). Post-volcanic hydrothermal activity and continuous CO_2-rich outgassing have resulted in pervasive alteration of the igneous rocks (serpentinites and dacites).

The Methana volcano comprises an ensemble of domes dated from 0.9 million to a few thousand years BCE, although activity may have begun during the Late Pliocene (Dietrich and Gaitanakis, 1995; Pe-Piper and Piper, 2002, 2013; Smet, 2014). The most recent eruptive episode has been described by Strabo and has taken place in approx. 230 BCE. Peripheral to the volcano magmatic activity appears both on- and offshore. Evidence of onshore activity is found in Poros Island, in the form of a small (ca. 1km^2) andesitic outcrop with composition similar to that of the Aegina volcanics (Mitropoulos, 1987; Francalanci et al., 2005). Evidence of offshore activity has been identified a few kilometres to the NW of Methana peninsula, where andesitic lavas have been dredged, having an age of approx. 1Ma as estimated on the basis of the thickness of the sedimentary cover (Papanikolaou et al., 1988). This is the site of the Pausanias submarine volcano, where short-lived extrusive activity has also taken place in 1700 CE. Contemporary activity in the Methana Volcanic Complex is limited to geothermal springs along the coastline, usually at locations associated with faulting (e.g. Dotsika et al., 2010). In addition, there is one thermal spring in the area of Hermioni, with temperatures of the order of 20–40°C. The heat flow map published by IGME (Taktikos, 2001) indicates high rates (70-150 mW/m^2) at Methana Peninsula, intermediate rates (50-70 mW/m^2) at south Argolis, and relatively low rates (30-50 mW/m^2) at the north and central Argolis.

2.4 Pre-Alpine Ultra-mafic Rocks

The study area has a complex geological structure comprising small outcrops of pre-alpine formations mainly at the south (e.g. Hydra Island), various alpine series of the Pelagonian zone, small outcrops of Mesozoic limestones of the Parnassus zone around (37.8°N, 22.8°E) and Plio-Pleiostocene sediments related to the CR at the north (Fig. 2). The stratigraphy, sequence and (tectonic) placement of these formations are of no consequence to the present analysis and will not be elaborated. The study area is also characterized by the presence of ultramafic formations (ophiolitic mélange) which are very important. These appear as patches outcropping along a broad N-S zone from Crommyonia (Megaris peninsula) to South Argolid (Hermionis area).

The Crommyonian (or Gerania) ophiolites have generally not been extensively studied. Recent work (Kaplanis et al., 2013) indicates that they have been emplaced by thin-skinned thrusting over the

Pelagonian margin during the Early Cretaceous (Eohellenic tectonic phase). This process has dismembered the ophiolitic complex so that the Crommyonian outcrop is essentially a (thin) nappe consisting mainly of serpentinized harzburgites. The magnetic susceptibility of the outcrop was measured in-situ at 10 different locations and varies between 6×10^{-3} and 15×10^{-3}, with a mean of 11×10^{-3} and a median of 11.55×10^{-3} (Efstathiou, 2011). It follows that magnetic anomalies would be significant only if the outcrop was massive and of large depth extent. The ophiolites are closely related to the Boeotian flysch which is essentially a mélange consisting of ophiolite-derived turbidites.

The ophiolitic outcrops of the Argolid have attracted considerable attention. According to Gaitanakis and Photiades (1989) there are three ophiolitic units. The lower unit is a Late Jurassic ophiolitic-sedimentary mélange thrusted on Late Triassic – Early Jurassic carbonates (Didyma – Trapezona formation). The intermediate unit comprises a series of dolerites, ultramafic lavas and cherts, formed by superficial thin-skinned overthrusting of oceanic crust onto the lower unit during the Late Jurassic – Early Cretaceous (Eohellenic tectonic phase). Finally, the upper unit is an ophiolitic tectonic mélange (harzburgites, serpentinites, gabbros, amphibolites, andesitic lavas in a schistose serpentinine matrix), thrusted on Late Cretaceous – Ypresian carbonates at the end of the Eocene. According to Gaitanakis and Photiades (1991, 1993), the most conspicuous and massive ophiolitic formations are those of the upper unit which is also characterized by suprasubduction related geochemical signature as well as extensive alteration and static greenschist metamorphism. Gaitanakis and Photiades, (1991, 1993) posit that in the SW Argolid, the ophiolitic mélange enriched with basalt fragments was thrusted on the crystalline basement (volcano sedimentary sequence) during the Late Jurassic and not on a carbonate platform as in the north and central Argolid. All ophiolitic formations are serpentinized and more or less weathered, altered and fragmented. These processes are detrimental to the magnetic susceptibility which varies from 0.02×10^{-3}–0.06×10^{-3} in the radiolarites and the matrix of the mélange, to 0.1×10^{-3} – 10×10^{-3} in heavily weathered/altered samples and to 20×10^{-3} – 36×10^{-3} in healthier samples (Efstathiou, 2011). Such susceptibilities indicate that the ophiolitic formations should not generate large amplitude magnetic anomalies, unless they are massive and of great depth extent.

3. Contemporary stress field and seismotectonics

Geological and tectonic mapping has not yet produced field evidence of the contemporary stress field in the study area, while reliable earthquake focal mechanisms have been rare until year 2002. As of that time, the establishment of the expanded Hellenic Unified Seismological Network (HUSN) and the installation of the ATHENET network by the University of Athens (as part of its contribution to the HUSN), have enabled continuous monitoring of the area with a sustainable detection threshold of at least $M \approx 1.5$ (e.g. D'Alessandro et al., 2011), as well as the determination of reliable focal mechanisms with advanced techniques based on full waveform inversion. Table 1 is a list of all hitherto known and well constrained focal mechanisms of *crustal* ($D < 30$km) earthquakes located in the broader study area. Fig. 3 illustrates the equal-area (Schmidt) projections of post-1990 mechanisms, i.e. only those determined by full waveform inversion techniques. Quite apparently, the number, diversity, geographical and magnitude distribution of the latter 33 mechanisms are adequate to warrant estimation of the crustal stress field by inversion, at least to a first approximation.

Let the stress field be defined in the standard geological/geophysical sense with $\sigma_1 > \sigma_2 > \sigma_3 > 0$ representing the principal stress axes. Then, the relative magnitude and orientation of the stress axes

can be computed from focal mechanisms by *formal inversion*, i.e. by finding the stress tensor that optimally reproduces the observed focal mechanisms. The stress field inversion method implemented herein is the SATSI algorithm of Hardebeck and Michael (2006), as redesigned and recast into the MSATSI software package by Martínez-Garzón et al. (2014). In fact, SATSI is an upgraded version of the method of Michael (1984, 1987) and uses a bootstrap resampling method to calculate misfit and home into the optimal solution. According to Hardebeck and Haucksson (2001), this approach is more accurate for noisy data sets and provides a more appropriate estimate of uncertainty. The inversion also returns a measure of the misfit between the optimal (best fit) solution and the data; this is given by the angle $\bar{\beta}$ which is the mean of the angles β formed between the calculated slip vector from stress tensor inversion and the observed slip vector from fault plane solutions. A synthetic control study showed that the amount of heterogeneity in the stress field could be characterized by means of $\bar{\beta}$: For focal mechanism data with errors of the order 10°-30°, $\bar{\beta}$ varies in the range 30°-45° when the spatially uniform and variable parts of the stress field have equal sizes (Michael, 1991). Thus, misfit angles significantly lower that these values can be taken to indicate satisfactory solutions and approximately homogeneous stress fields.

Conditions for the results of formal inversion to be meaningful are: (a) the stress should be uniform in the study area, at least during the interval in which the data was acquired; (b) the earthquakes under consideration should be shear dislocations on pre-existing faults; (c) similar shear stress magnitude should be present at each fault and, (d) the slip should occur in the direction of the resolved shear stress on the fault plane. Accordingly, the inversion was carried out on the basis of 22 post-2002 events with moment magnitudes between 3.8 and 4.9 and yielded a misfit $\bar{\beta}$ = 18.6 ± 15.7. This is not exceptional but it is based on more than 15 well constrained single events in close geographic proximity and with a misfit of less than 20° can be classified as borderline between Quality A and B, according to the ranking scheme of Zoback and Zoback (1989, 1991) as refined by Sperner et al. (2003) and used by World Stress Map Project. A graphical representation of the expected crustal stress result is shown in Fig. 4: The principal compression axis σ_1 is oriented at N64° and plunges at 77° (open square), while the principal extensional axis σ_3 is oriented at N210° and plunges at 10° (open circle). The stress field is mainly extensional, NNE-SSW oriented and overall homogeneous. The "typical" focal mechanism generated by this field is shown with thick black lines and a schematic depiction of the faulting pattern predicted by Riedel's shear theory is also superimposed.

According to the results above, the expected principal direction of normal faulting is WNW-ESE (approx. N290°) for north-easterly dipping faults and NW-SE (approx. N130°) for south-westerly dipping faults. The former is spectacularly manifested in the hanging cliffs of the northern coast of Argolis peninsula, as well as in identically oriented normal faults mapped by Papanikolaou et al. (1988) within the Saronic Gulf. This result is also consistent with the findings of Papanikolaou and Lozios (1990), while Drakatos et al. (2005) have mapped a similarly oriented lineament of crustal earthquake foci between Methana peninsula and Aegina Island, collocated with faulting structures mapped by Papanikolaou et al. (1988). The latter faulting direction is observed mainly offshore, along the northern margin of the Argolic, between Spetsai Island and the head of the gulf (Papanikolaou et al., 1988; VanAndel et al., 1993). It is also inferred to extend onshore, flanking the eastern margin of the Argolic Plain. In addition, the results predict the existence of W-E faults consistent with the synthetic (dextral) R-shear direction of Riedel's shear theory and NW-SE (approx. N330°) faults consistent with the antithetic (sinistral) R´-shear direction. The configuration of the stress field allows

for a small ENE-WSW compressional component which may easily account for local-scale faulting with significant lateral heave. Indeed, active, oblique-normal (transtensional) faulting consistent with the expected R and R´ directions can be seen to exist in a few focal mechanisms of small earthquakes observed in the southern Argolid and the Argolic Gulf (Table 1 and Fig. 3). More detailed analysis of the significance of the results –and the significance of lateral-slip faulting in particular– is deferred to Section 5 (Discussion and Conclusions) where seismotectonic, aeromagnetic and other geological evidence is jointly interpreted. The above stress configuration requires the existence of crustal-scale WSW-ENE (N70° – N80°) regional shearing deformation which, we assume, is accommodated in the background SW-ward translation of the Aegean plate. It is also worth mentioning that this orientation is parallel to the orientation of the WSW-ENE shear structures investigated in central Greece by Tzanis et al. (2010), indicating that it may be part of a broader deformation pattern.

4. Aeromagnetic data analysis

4.1 Aeromagnetic data

The aeromagnetic data used herein have been extracted from the recently (re)compiled aeromagnetic map of Greece (Chailas et al., 2010) as augmented by Efstathiou (2011). These authors attempted to generate a unified, homogeneous and common-referenced aeromagnetic map of Greece, out of the fragmentary information existing in a multitude of 1:50000 scale maps produced by different contractors for the Institute of Geological and Mineral Exploration (IGME). With respect to the study area, the compilation was based on the 1:50,000 map series produced by Hunting Geology and Geophysics Ltd for areas C3 (Eastern Central Greece) and D2 (Central Peloponnesus). Hunting has generally used a measurement spacing of 200–250m along track and has always flown in a NE-SW direction (approx. N45°), but at different ground clearances (GC) and track densities, depending on the topography: Area C3 was measured at a nominal GC of 300m above ground level (AGL) and nominal distance of 800m between tracks; Area D2 was measured at a nominal GC of 2000m above mean seal level (AMSL) and a nominal distance of 1000m between tracks. In both cases, connection lines were flown in a SW-NE direction and 10km spacing between tracks.

The original 1:50000 map sheets were converted to high resolution raster images and digitized to vector form in image coordinates. Using the corners of the map sheets as control points, the image coordinates were geo-located and transformed to Cartesian in the UTM projection. The digitized data was finally interpolated to a rectangular grid with a uniform spacing of 250m, so as to generate Digital Aeromagnetic Anomaly Models (DAAM) for Areas C3 and D2 respectively. The two DAAMs were subsequently "homogenized" by referencing to a common clearance AGL. Because the DAAM of Area C3 is by far the major source of data, we have chosen to downward-continue the DAAM of Area D2 to a constant clearance of 300m AGL. This is an exercise in field continuation between arbitrary surfaces and has been carried out with the efficient equivalent sources method of Xia et al. (1993). Details of the procedure can be found in Chailas et al. (2010). The DAAM of Area C3 and the downward-continued DAAM of Area D2 were collated to generate the aeromagnetic anomaly map shown in Fig. 5a, which was next reduced to the North Pole for subsequent analysis (RTP-DAAM, see Fig. 5b).

As is evident in Fig. 5a, the suture between Areas C3 and D2 is not seamless and can be identified in the SW quadrant of the DAAM, as well as between Easting 650-660 and Northing 670-680. The offset has variable amplitude and is presumably generated by systemic factors such as levelling error, raw data processing and imperfect continuation. One may also observe flight-line artefacts (levelling error) appearing as lineation or striation at an azimuth of N45°. These flaws are inherited from the original aeromagnetic map and are still present in the RTP-DAAM, although flight-line artefacts are not clearly seen in Fig. 5b. Nevertheless, they exhibit rather low amplitudes and are highly localized in space, so that their effects should be significant only at long to very long wavenumbers, within the realm of noise. In consequence, they are not expected to have any measurable effect on the results.

4.2 General characteristics of magnetic sources

A semi-quantitative approach to the analysis and interpretation of aeromagnetic data is to study the scale and distribution of magnetized geological formations (sources) with depth and to separate, if possible, magnetic anomalies generated by ensembles of sources located at different depths. This exercise customarily implements spectral methods in the Fourier plane and specifically the analysis of the *radially averaged power spectrum* pioneered by Spector and Grant (1970). Note, however, that because offshore areas had been excluded from the original aeromagnetic survey, there are significant expanses of missing data. It is therefore necessary to condition the data in order to suppress spurious effects that would inevitably accompany Fourier transformation. This is done heuristically: the void grid nodes are assigned with a value equal to the arithmetic mean of the unified RTP-DAAM plus 5% white noise. In this way, after the mean is subtracted for Fourier transformation, the missing data areas will assume the role of purely random variation at very long wavenumbers and will not interfere with the spectral structure of the geological magnetic sources. Gibbs effects and oscillatory aliases are suppressed by padding the RTP-DAAM with zeros to thrice its initial size: if the RTP-DAAM matrix is $M \times N$, the padded matrix is $3M \times 3N$.

Fig. 6 illustrates two realizations of the radially averaged power spectral density derived from the RTP-DAAM vs. the radial wavenumber k. The radial averaging is performed by partitioning the Fourier plane into concentric circular or rectangular annuli and taking the expectation value of all power spectral realizations within each annulus. The two realizations shown in Fig. 6 were obtained with different partitioning schemes, resulting in different resolutions of the radial power spectral density. A somewhat unexpected observation in both realizations is that the basal (deepest) ensemble of magnetized structures is depth-unlimited, whereas a depth-limited layer was expected on the premise that the Curie isotherm would be elevated at the vicinity of the Hellenic Volcanic Arc. Notably, Tselentis (1991) has determined a Curie isotherm depth of the order of 12–15 km for the broader area of the Argolid, excluding the Saronic Gulf and the Methana Volcanic Complex. A plausible explanation, indirectly corroborated by the ensuing analysis, is that several basal sources are laterally extended and transcend the area of aeromagnetic observations, so that their floor cannot be constrained. A second important observation is the absence of conspicuous long straight line segments in the radial spectrum. The absence of transient (high-amplitude/ localized) features in the RTP-DAAM, as well as high-amplitude laterally extended shallow sources and high-amplitude step-like discontinuities, precludes broadband contamination of the wavenumber spectrum. As a consequence, the shape of the radial spectrum indicates that the sources located above the basal layer are distributed over almost all depths. This excludes spectral methods that examine isolated magnetic anomalies (e.g.

Bhattacharyya and Leu, 1975) and compels the implementation of methods based on statistical physics, e.g. as in Spector and Grant (1970).

Although magnetic sources are not concentrated in "layers" with distinct ceilings and floors that can be determined by standard straight line fitting methods, it is still possible to extract useful information and valuable insight. Following the formulation of Spector and Grant (1970), we approximate the radially averaged spectrum with one depth-unlimited and four depth-limited ensembles of magnetized sources using the parametric function

$$\hat{P}_r(k) = A_1 e^{-2kZ_1} + \sum_{j=2}^{5} A_j k^2 e^{-2kZ_j} + A_n \qquad (1)$$

where A_j are the ensemble strengths, Z_j are the depths to the tops of the ensembles and A_n is the noise level. We determine the parameters of Eq. (1) with non-linear least squares by minimizing the loss function $\left\| \log P_r - \log \hat{P}_r \right\|^2$ subject to the constraints $A_j > 0, \quad Z_j > 0, \quad A_n > 0$. The procedure generates families of excellent best-fitting models with $R^2 > 0.99$, such as those shown Fig. 6.

A simple inspection of Fig. 6 shows that the depth to the basal layer is inconsistently determined and is also associated with large confidence intervals. In fact, the determinability of the strength and depth to the basal layer is very sensitive to the averaging scheme with which the radial spectrum is calculated; this affects the resolution of short wavenumbers so that broader averaging annuli (lower resolutions) would bias the solution to shallower depths and vice versa. Conversely, the depths to the shallower (depth-limited) ensembles are rather consistently determined in both higher and lower resolution power spectral realizations because their localization is less sensitive to the averaging scheme. Because non-linear least squares solvers are local, it is also easy to ascertain that different starting models (A_j, Z_j, A_n) may easily result in different estimates of the depth to the basal layer even for the same realization of the radial spectrum. However, and as will become abundantly clear in Section 4.3, the determination of trustworthy parameters for the basal layer is very important. In consequence, the problem of finding maximum likelihood estimates of the parameters A_j, Z_j and A_n must be treated statistically. The solution given herein implements a bootstrapping approach as follows: Random realizations of the radial spectrum are generated, to which random starting models are assigned and used by the non-linear least squares solver to find a best fitting (local) solution. The process is repeated many times over so as to generate large populations of strength estimates $\{\hat{A}_j\}$, depth estimates $\{\hat{Z}_j\}$, and noise estimates $\{\hat{A}_n\}$, each associated with 95% confidence intervals $\{\delta\hat{A}_j\}$, $\{\delta\hat{Z}_j\}$ and $\{\delta\hat{A}_n\}$ respectively. Finally, the expectation values $\langle A_j \rangle$, $\langle Z_j \rangle$ and $\langle A_n \rangle$ are estimated in a least-squares sense as $\langle X_j \rangle = \sum\{\hat{X}_j w_j\} \big/ \sum\{w_j\}$, with $\{w_j\} = \{1/\delta\hat{X}_j\}$. Fig. 7 illustrates depth estimates obtained after 1000 iterations of the procedure; Table 2 presents the final expectation values obtained after 5000 iterations. The depth to the basal layer exhibits the expected variability, nevertheless, the weighted average $\langle Z_1 \rangle$ appears to be a fair compromise and leans towards the higher density of $\{Z_1\}$ determinations, implying that estimates greater than 7.5-8km are generally associated with larger errors. Approximately 72% of $\{Z_1\}$ lies within one standard deviation of the expectation value. This leaves a small population of upward biased (> 8km) determinations to form what appears to be their own distribution. All the other depth populations $\{Z_2\}$ to $\{Z_5\}$ are consistently determined. Analogous results are obtained for the strengths $\{A_j\}$ but are not shown for the sake of brevity.

The final results indicate that the *basal* (depth-unlimited) sources are located at depths greater than approx. 7 km *below flight level* (BFL). In terms of power, the most significant contributions to the magnetic anomaly map appear to be made by large scale sources buried deeper than 4km BFL. These will henceforth to be referred to as *deep* structures and will receive particular attention in the ensuing analysis. Smaller contributions are made by an ensemble of *shallow* structures extending between 0.3 – 1.8 km BFL, or 0 – 1.5 km below the surface. These are generally local and as will be seen shortly, they may be attributed to ophiolitic and volcanic formations, either buried or outcropping. Some of the shallow sources also appear to be genetically related to the deep ensemble in the sense that they comprise extensions of deeper structures, as for instance in the vicinity of the Methana Volcanic Complex. The remaining of this section is devoted to the separation and examination of anomalies generated by the deep and shallow structures using the efficient anomaly separation scheme introduced in Appendix I.

4.3 Separation of anomalies according to source depth

The results of the "anomaly separation" exercise are shown in Fig. 8-11 and have all been obtained with the Radial Extended Meyer Window filter described in Appendix I. Fig. 8 illustrates the large-scale anomalies generated by the *basal* geological sources (depths greater than 6.8-7 km). Two main anomalies of comparable amplitude can be observed: one developing beneath the east coast of the Peloponnese in the west, and one along Methana VC – Cape Skillaion line, (*Skl* – M*VC* in Fig. 8), exhibiting overall NW-SE elongation,. A relatively low-amplitude (approx. 10nT) anomaly elongated in the W-E direction appears to develop beneath Crommyonia and Megaris (*CM* in Fig. 8). The *Skl* – *MVC* – *CM* anomalies are aligned on the 100km contour of the subducting slab. This is consistent with the depths at which low-temperature and high-pressure mineral phase transitions involving the growth of dense anhydrous minerals (garnet and eclogite), drive water out of the slab and into the mantle wedge, thereby initiating flux-melting processes that generate andesitic magmas and give rise to arc volcanism (e.g. Grove et al., 2006 and references therein). The basal anomalies are truncated, as they extend beyond the boundaries of the aeromagnetic survey. As a result, their large-scale geological source formations cannot be effectively constrained; this may be a plausible explanation as to why they appear to be depth-unlimited in the radially-averaged power spectrum although they certainly lose their magnetization at depths 12–14 km (depth to Curie isotherm).

Fig. 9 illustrates the anomalies generated by the deep depth-limited source ensembles and specifically those located at depths between 7 and 4 kilometres BFL. These are generally of lower amplitude (up to 65 nT) but larger scale and appear to be arranged in two distinct orientations:

- Approx. N310° – N320° parallel to the east coast of the Peloponnese and along the axis of the Argolic Gulf (marked *AG* in Fig. 9), as well as between Cape Skillaion, Methana VC and Crommyonia (*Skl – MVC – Dhi* line of Fig. 9). Notably, the former (*AG*) anomalies are roughly aligned with the surface projection of the 60km isodepth; the significance of this observation will be discussed in Section 5 under the light of additional information. The latter anomalies are roughly but conveniently aligned with the 100km isodepth of the subducting slab. Attention is also drawn to the Dhiaporian islet anomaly, (*Dhi* in Fig. 9), which appears exclusively undersea in the Gulf of Megara and is tightly framed by faulting structures.

- Approx. W-E between the areas of Epidavros and Methana VC (*EDA – MVC* in Fig. 9), as well as along the Argolic Gulf – Hermionis – Hydra Gulf – Cape Skillaion axis (*AG – Her-HdG – Skl* in Fig. 9).

Fig. 10 illustrates *intermediate* anomalies generated by sources buried between 4 and 2 kilometres BFL. These are significantly more localized and of slightly larger amplitude in comparison to the deep-source anomalies (up to 100 nT), except in the area of the MVC where amplitudes rise to approx. 200nT. Specifically, one may observe:

- Alignments of N310° – N320° orientation along the axis of the Argolic Gulf (*AG*), collocated with the trace of the 60km isodepth of the subducting slab, as well as along the axis Cape Skillaion (*Skl*) – Poros Island (*Por*) – Methana (*MVC*) – Dhiaporian Islets (*Dhi*) and Crommyonia (*CM*), collocated with the 100km isodepth of the subducting slab (see above). A rather low amplitude (up to 30nT) alignment of localized anomalies with similar orientation develops to the NW of Hermionis, along the east coast of the Argolic Gulf between coordinates (E641, N680) and (E667, N670); it is indicated with a series of question marks.
- Alignments of approx. W-E orientation along an axis through the Argolic Gulf (*AG*), Hermionis (*Her*), Hydra Strait (*HdS*) and Cape Sklillaion (*Skl*), as well as between Epidavros (*EDA*) and Methana (*MVC*). The latter is apparently associated with the deep *EDA – MVC* anomaly, which would appear to split into two localized features (*EDA* and *MVC*) at intermediate depths. A rather significant anomaly of approx. 140nT at peak is observed at the area of Radon (*Rd*). This appears isolated although there is strong indication that it may be connected to the Poros Island anomaly (*Por*) via a low amplitude anomaly of approx. 15nT through the area of Kalloni (*Kl*). Finally, an alignment of localized sources with relatively low amplitudes (up to 60nT) and roughly W-E orientation appears at approx. 680N and 670E – 710E, apparently bracketed by two lineaments of similarly oriented faults.

The *Dhi* anomaly can also be observed at intermediate depths with a maximum amplitude of 60–70nT. It is again tightly framed by faults but is now stretched in an N-S direction, apparently in response to the corresponding stretching of the causative body and presumably in association with the N-S component of the framing fault system. A localized, N-S oriented anomaly of similar amplitude also appears at the area of Crommyonia (*SO*). Signatures of intermediate sources that are *not* observed at depths greater than 4km appear at Kalloni (*Kl*), Radon (*Rd*), along the east coast of the Argolic Gulf (marked as "*?*") and Crommyonia (*CM*). Some of these may be due to recent igneous intrusions. Some intermediate anomalies appear at areas adjacent to, or coinciding with Mesozoic ophiolitic outcrops; examples of the former can be seen at Epidavros (*EDA*) and Hermionis (*Her*), while characteristic example of the latter is Radon *(Rd*). These anomalies will be discussed in Section 5, after additional information is presented. As a general rule, however, the deep and intermediate sources (2km < Z < 7km) are arranged in distinctive W-E and NW-SE (N310°–N320°) configurations, are generally massive and are spatially correlated with extensional tectonic structures and the Hellenic Volcanic Arc as in the case of the *Skl – Por – MVC – Dhi –CM* alignment. This clearly distinguishes them from the shallow-buried (Z < 2km) sources which are generally distributed and of local scale, as will be shown forthwith.

The final Fig. 11 illustrates magnetic anomalies, associated with shallow (but not superficial) sources (0.3km < Z < 1.8km). These are generated by a complex of distributed near-surface formations consisting of buried or extrusive volcanics and outcropping or shallow-buried ophiolites. The highest

amplitudes (100 – 720 nT) are observed in association with the extrusive volcanics of Methana peninsula while the ophiolites, on account of being generally altered and weathered, are associated with appreciably lower amplitude anomalies (20 – 150nT in general and up to 240nT at Epidavros).

The distinctive NW-SE and W-E configuration of the deep and intermediate sources cannot be observed at their respective locations and is replaced by a pattern of distributed, local, low-amplitude anomalies, as for instance along the Argolic Gulf and along the Hermionis Peninsula – Hydra Gulf – Cape Skillaion line. In many cases, such anomalies could be attributable to intrusive activity, particularly in the neighbourhood of the Methana Volcanic Complex (MVC). The high-amplitude Methana anomalies are principally associated with the central domes of the volcanic edifice (up to 700 nT), the distinctive lava flow of the 230 BCE eruption at the immediate NW of the central domes (approx. 725nT) and the Pausanias submarine volcano (*Ps* in Fig. 11), right to the NW of the peninsula. Additional, anomalies related to the MVC include the areas of Kalloni (*Kl*) and the Poros-Troezenia strait where the anomaly is directly associated with a small andesitic outcrop (Poros andesite). Three small scale anomalies appear at the location of the deep Dhiaporian Islets anomaly (*Dhi*); these may be offshoots a deeper seated pluton. The localized low amplitude (< 40nT) anomaly marked *ATD* is the signature of the small dacitic outcrop found at the Aghioi Theodoroi area of Crommyonia. Moreover, the area of the Sousaki solfatara does not appear to generate any significant magnetic signature.

Ophiolite outcrops generate distinctive magnetic signatures. The Epidavros ophiolites (*EO*) produce a significant anomaly that is clearly delimited by the outcrop, while the Gerania (*GO*) and other Crommyonian ophiolites exhibit a patchwork of rather low amplitude anomalies (< 70nT), also completely delimited by the outcrops. Conversely, the Fournoi – Heliokastron anomaly (*HlO*) extends to the east of the outcrop, its source presumably buried under the Pelagonian flysch. A low amplitude anomaly (< 100nT) also develops around the small outcrop of Nea Epidavros, to the SE of *EO* and the Radon outcrop (*RdO*) is also collocated with a 150nT anomaly which extends beyond the boundaries of the outcrop. The anomalies associated with the Hermioni ophiolites (*HrO*) are clearly insignificant. It is also worth noting that the outcrops of South Argolid ophiolites (*RdO* and *HlO*) are characteristically elongated in the W-E direction and correlated with local W-E tectonic lineaments. We shall argue in Section 5, that is a result of tectonic activity, possibly the same as the one that modulated the configuration of the deep sources.

5. Discussion and Conclusions

Herein we examine aeromagnetic data collected over a broad area of Northeast Peloponnesus, (Argolid, eastern Corinthia and the Argolic and Saronic gulfs), for evidence of deep and shallow calc-alkaline syn-rift magmatism related to the broader Corinth Rift system and the Hellenic Volcanic Arc. The analysis is semi-quantitative: in a first step we identify ensembles of magnetized geological bodies (magnetic field sources) buried at different depths with parametric modelling of the radially averaged power spectrum; in a second step we use a bank of efficient, automatically scalable wavelet filters to separate the anomalies associated with these ensembles and evaluate their configuration, extent, nature and contribution to the composition of the total (aero)magnetic intensity map of the study area. A cardinal part of our work is to evaluate the relationship between the different magnetic source ensembles and the active tectonics of the study area, as a means of inferring their nature, origin and current disposition. To this effect, we also evaluate the contemporary stress field –hence the

expected faulting pattern– with formal inversion of all known and well-constrained earthquake focal mechanisms and interpret the existing neotectonic ken under the light of our findings.

5.1 Contemporary Crustal Deformation

According to the analysis of Section 3, the expected principal direction of normal faulting modes in the study area is WNW-ESE (N290°), which is mainly observed along the northern coast of Argolis peninsula and in the Saronic Gulf, and NW-SE (N130°) mainly observed in offshore faults along the northern margin of the Argolic Gulf, between Spetsai Island and the head of the Gulf. An interesting outcome of the same analysis is the recognition of local-scale W-E and NW-SE (N330°) oriented faulting, respectively consistent with the synthetic (dextral) R-shear and antithetic (sinistral) R´-shear directions of Riedel's shear theory. The latter may comprise a significant component of local crustal deformation, as we discuss below.

W-E faults have been mapped by various authors both onshore and offshore in the Argolic and Saronic gulfs; a very interesting such feature is the well-defined offshore alignment of epicentres between Aegina and Salamis islands detected by Drakatos et al. (2005), which has been interpreted to comprise a southerly extension of the Gulf of Corinth (GoC) normal fault system. According to our results, the W-E faulting direction is consistent with the synthetic (dextral) R-shear direction. In this respect, it is plausible that at least in the area south of 38.7 °N, the W-E faults are more than just southerly expressions of the GoC normal faults. Rather, they may comprise structures inherited from the inception of the Corinth Rift (hence related to the GoC system), but which have evolved to accommodate the strain differential caused by the apparent disparity of extensional trends in the Argolic and Saronic gulfs by developing non-trivial right-lateral heave. It is also conceivable that the W-E faults are oblique-normal (of transtensional nature), as can be observed in a few focal mechanisms of the southern Argolid and the Argolic Gulf (Table 1 and Fig. 3). The origin of the different extensional trends in the Argolic and Saronic gulfs is yet to be specified and we note that this problem will be revisited in follow-up work and will be addressed with additional observational data.

Faults of NW-SE (approx. N330°) orientation, parallel to the antithetic (sinistral) R´-shear direction have rarely been mapped in the Argolid with the possible exception of onshore and offshore features observed in the vicinity of the Methana volcanic complex (also see Papanikolaou et al., 1988). Note, however, that this orientation is almost parallel to the strike of the Argolic Gulf and Plain, the east coast of Peloponnesus and the faulting structures observed therein (SW quadrant of Fig. 3). It is also parallel to the local trend of the Hellenic Volcanic Arc and the subducting slab (e.g. Fig. 1; also see Suckale et al., 2009 and references therein). Accordingly, it should not be dismissed as it may represent some kind of coupling between the rapidly southwesterly-moving Aegean continental forearc and the slowly northeasterly-subducting slab.

5.2 Deep Magnetic Anomaly Sources: Origin and Relationship to Regional Tectonics and the Hellenic Subduction.

The analysis presented in Section 4 indicates that magnetic field sources buried at depths greater than 2 km are clearly distinguishable from those buried at shallower depths. The former comprise generally elongate and massive formations arranged in a distinctive W-E and NW-SE (N310°–N320°) configuration; these are spatially correlated or bracketed by the major extensional or transtensional

neotectonic structures, or are directly located on the Hellenic Volcanic Arc (along the axis *Skl – Por – MVC – Dhi –CM* of Fig. 8 and 9, which includes two known volcanic fields). Given that the ophiolites generally comprise dismembered thin nappes of tectonic mélange emplaced by thin-skinned overthrusting and are thus unlikely to generate significant deep-seated magnetic anomalies, it is plausible that the deep and intermediate sources are actually magmatic intrusions (dioritic – granodioritic plutons) whose placement is, or has been controlled by *syn-rift* tectonic activity. Intermediate depth (2km < *Z* < 4km) sources are generally more localized than the deep sources (4km < Z) but this is not difficult to explain: if they are of igneous origin, then the intermediate sources should be localized extensions of the deep sources formed by ballooning, wedging or branching of the main plutons toward the surface. Sources buried at depths shallower than 2km are generally local and distributed, in most cases directly identifiable with ophiolitic outcrops and extrusive calc-alkaline volcanics (also see below). There are, however, some "grey areas" in the depth interval 2 – 3 km, where the extensions of the deep (plutonic) sources may overlap or even merge with the deeper roots of shallow sources. We shall now proceed to justify our interpretation and discuss the nature and disposition of the magnetic field sources, with particular reference to the deeper ensembles.

The surface of the study area features two types of geological formations capable of generating significant magnetic anomalies: ophiolitic mélange and calc-alkaline extrusive rocks (andesites to dacites) associated with the Methana Volcanic Complex. As found by Efstathiou (2011) the magnetic susceptibility of the ophiolitic formations averages to 11×10^{-3} with a median of 2×10^{-3} and range of 0.02×10^{-3} – 36×10^{-3}. Respectively, the susceptibility of the extrusive volcanics averages to 20×10^{-3} with a median of 17×10^{-3} and a range of 5×10^{-3} – 26×10^{-3}. The ophiolitic mélange has formed in accretionary prisms and obducted onto its present position by gravity sliding (olistostromes), or by thin-skinned overthrusting. The Gerania (Crommyonian) ophiolite outcrop is associated with low amplitude (< 80nT) anomalies, as one would expect of a rather thin nappe consisting of serpentinized harzburgites, with magnetic susceptibilities no higher than 15×10^{-3}: it can safely be concluded that the thickness of the Crommyonian ophiolites is significantly smaller than 1 km, so that any anomaly generated by sources under this depth could be attributed to igneous (dacitic) intrusions. The mélange of the north and central Argolid consists of radiolarites intercalated with 10-30 m thick ophiolitic olistostromes comprising agglomerates of medium-sized ophiolitic olistolites and having undergone static greenschist metamorphism. Chaotic deposition, metamorphism and chemical alteration associated with the depositional environment generally diminish or even completely destroy magnetic susceptibility, as confirmed by the measurements. The mélange of the southern Argolid consists of a schistose serpentinitic matrix with medium to large size ophiolitic blocks and apparent thicknesses of up to 200 m (Gaitanakis and Photiades, 1991, 1993). This unit is also characterized by suprasubduction related geochemical signature as well as extensive alteration and static greenschist metamorphism, all of which account for the low magnetic susceptibilities measured by Efstathiou (2011), even in the healthier (least weathered) rock samples. Several magnetic anomalies generated by sources shallower than 2 km can be directly identified with ophiolitic formations in the Argolid (Fig. 10). These are the Epidavros Ophiolites (*EO*, with amplitude up to 300 nT), the Radon Ophiolites (*RdO*, up to 240 nT), the Heliokastron Ophiolites (*HlO*, up to 150 nT) and the Hermioni ophiolites (*HrO*, up to 130 nT). These amplitudes can be safely attributed to the physical characteristics (apparent thicknesses and susceptibilities) of the ophiolitic mélange, as determined by surface observations. As can be easily demonstrated by analytic continuation and without factoring in the demagnetizing effect of the geothermal gradient, if the respective ophiolitic formations were buried at

depths of 2.5 km or 4 km, they would generate anomalies no higher than 40 nT and 16 nT which are at least 50% lower than the lowest amplitude attributed to intermediate and deep sources (Fig. 8 and Fig. 9). Conversely, if deeply buried ophiolitic formations were to account for the observed deep-source anomalies, they would either have to be forbiddingly massive with respect to their observed physical characteristics and emplacement process, or they would have to have much higher susceptibility (i.e. different composition).

In continuing our discussion of the sources of magnetic anomalies in the study area, we note that well-informed researchers (e.g. D. Piper, 2016, personal communication) have contemplated the possibility of magnetic anomalies being –partially at least– generated by Triassic lavas (represented by thin pyroclastics at Epidavros), or Hercynian plutons in the Pelagonian basement (e.g. as summarized in Ch. 2 of Pe-Piper and Piper 2002). The former rock formation has been described by Gaitanakis and Photiades (1991) as consisting of olistolites of lavas and radiolarites with diameters generally smaller than 30 cm, embedded in turbiditic volcano-sedimentary formations with apparent thicknesses of 40 m on average. The nature of these formations suggests that as with the ophiolites, their igneous material should have undergone extensive processing and alteration and should be largely demagnetized. In support of this assessment, we note that eastward of Vourlos bay (*VB* in Fig. 10 and 11), where such formations have been observed to outcrop, there are no magnetic anomalies at depths greater than 2 km (Fig. 10) and very weak anomalies, of the order of a few nT, at depths shallower than 1.8 km (Fig. 11).

Massive granitoid plutons in the Pelagonian basement are observed in the western and central Macedonia, Greece; these are dated to the Upper Carboniferous and are unconformably overlain by terrigenous metasediments of probable Permian to Middle Triassic age (e.g. Kotopouli et al., 2000; Pe-Piper and Piper, 2002). As can be easily verified by overlaying the geological (Kotopouli et al, 2000) and aeromagnetic (Chailas et al., 2010) maps of W. Macedonia, these formations are either completely non-magnetic as in the Pieria, Deskati and Olympiada complexes, or exhibit localized anomalies as in the case of the Varnountas pluton. Such massive basement plutons are not observed in the rest of the Pelagonian zone and their presence in the Argolid has never been established. Photiades and Gaitanakis (1991) have observed three small granodiorite outcrops with sizes not exceeding 50×10 m along the strike of the Koilada-Loutra-Thermisia fault zone (*KLT* in Fig. 9-11)**,** which they interpret to comprise fragments of the local Pelagonian crystalline basement. These, however, have been dated to the Mid-Late Jurassic on the basis of U-Pb igneous zircon dating (Photiades and Keay, 2000). Moreover, the geological field data provide no indication whatsoever as to the existence of sizeable granodioritic bodies beneath the outcrops (or beneath the entire Argolid for that matter). At depths between 7 and 2 km the *KLT* fault zone appears to form the northern boundary of the *Her-HdG* (Fig. 9), *Her* and *HdS* (Fig. 10) group of anomalies. Although one might suggest that these anomalies have been generated by "massive" basement plutons, we can argue that this is certainly not the case. Along the *KLT* fault zone and at depths shallower than 2 km there is absolutely no indication of shallow-buried magnetized rock formations and any anomaly observed to the north of the zone can be directly and exclusively attributed to the *HlO* ophiolitic suite (Fig. 11). This means that the granodiorite outcrops observed along *KLT* are either non-magnetic, or are very small and localized, lacking continuity and deeper roots. There are no studies of a possible relationship of the Argolid granodiorite basement outcrops with the massive Carboniferous Pelagonian plutons of western Macedonia and, given their vastly different sizes and ages, their correspondence cannot be asserted. Given also the largely non-magnetic nature of the Macedonian plutons and the apparently non-magnetic nature of the

Argolid Pelagonian basement's granodiorites, the plausibility of aeromagnetic anomalies generated by "massive" magnetized "ancient basement plutons" at depth cannot be entertained.

The magmatic nature and origin of the N310°–N320° and W-E oriented deep-source anomalies is all the more plausible because they are collocated with the axes of contemporary extensional (N310°–N320°) or transtensional (W-E) neotectonic structures and the N310°–N320° oriented Hellenic Volcanic Arc (HVA): let alone that rifting processes favour intrusive magmatism, it is rather difficult to dispute the magmatic origin of deep sources in the vicinity and along the HVA, as well as around the Methana Volcanic Complex. The relatively elevated heat flow of southern Argolid, 50-70 mW/m^2 according to Taktikos (2001), is consistent with this idea. The concept of recent plutonic activity could be strengthened by comparison with analogous Miocene plutonism in the Cyclades. As D. Piper (2016, personal communication) pointed out, this plutonism is in many places localised along major strike-slip faults, but with lighter granitic magmas ballooning out along mid-crustal extensional detachment surfaces. Mafic magmas are more abundant at deeper crustal levels (e.g. Delos). The crystallisation depth of the strike-slip related western granodiorite pluton of Naxos is fairly well constrained by mineralogy of the thermal aureole and geobarometry of hornblende to 1.5-2.5 kbar or 5-8 km (Pe-Piper, 2000), similar to the depths of the magnetic sources detected herein. Mafic enclaves are very abundant in some volcanic rocks on Methana (Pe-Piper and Piper, 2013) and are known at Crommyonia/Sousaki (where some of the oldest rocks are andesitic).

As mentioned above, it is rather difficult to contend the magmatic origin of deep magnetic field sources in the vicinity of the HVA. Conversely, it is necessary to illustrate the plausibility of the magmatic nature of deep sources along the axis of the Argolic Gulf and Plain. Fig. 12 shows the epicentral distribution of sub-crustal (> 40km) earthquakes observed over the broader study area and over the period 1965–2012. The data has been extracted from the on-line bulletin of the International Seismological Centre (http://www.isc.ac.uk); only earthquakes with $m_b \geq 3.5$ magnitudes are shown and plotted on their primary ISC location coordinates. The ISC catalogue was favoured because it is based on a large, trans-border observational data set and advanced hypocentre location techniques (Bondar and Storchak, 2011) that have also been used to relocate earthquakes since 1965. In comparison to the other definitive earthquake catalogues of the broader study area, the ISC bulletin provides the more complete and consistent source of deep seismicity information since 1965. Fig 13 is a composite SW-NE section across our study area. The bottom panel of Fig. 13 illustrates: a) The projection of the sub-crustal earthquake hypocentres of Fig. 12 on the profile AB of Fig. 12. b) The electrical resistivity cross-section along the profile CD of Fig. 12, rotated parallel to AB and projected on the AB plane; this information was extracted from the deep magnetotelluric profile of Galanopoulos et al. (2005) and was generously provided by Dr V. Sakkas and Dr E. Lagios of the University of Athens (personal communication). c) A profile of the Mohorovičić discontinuity of the Aegean plate according to Sachpazi et al., (2007), collocated with profile AB. d) A profile of the Mohorovičić discontinuity of the Aegean plate according to Suckale et al., (2009), rotated to the orientation of AB and projected on the AB plane. e) A profile of the ceiling of the subducting slab taken from the tomographic image of Fig.1 of Sachpazi et al., (2016), which is approximately collocated with the CD plane; this has been rotated to the orientation of AB and projected on the AB plane. The top panel of Fig. 13 is a vertically exaggerated topographic section along AB, together with major normal faults (as per Fig. 2).

The location of the subducting slab is clearly defined by the distribution of earthquake hypocentres. The light grey line envelops and approximately outlines the slab; it is a means of visualization enhancement and does not represent its true thickness. The slab dips eastwards at an *apparent* angle of 20° up to the Argolic Gulf and 40°-45° thereafter. An inflection appears exactly below the Argolic Gulf, at a depth of approx. 65km, consistently with Hatzfeld et al., (1989). Inflection has also been imaged at the *same* depth by the tomographic study of Sachpazi et al., (2016), along the CD plane. The size of an apparent dip angle depends on the orientation of the section along which it is measured. Simple calculations show that for the shallow dipping leg of the slab, the discrepancy is very small between the earthquake and tomographic data. For the steep-dipping leg however, it may account for up to 4° (~40%) of the difference observed in the plunges of the two profiles, the remaining being attributable to technical issues (methods of analysis) and the true geometry of the slab relative to the location of the two profiles. Section AB crosses the Methana volcanic complex and as can be readily observed the slab is located at approx. 110km beneath the volcano. This is consistent with the depth at which low-temperature and high-pressure mineral phase transitions involving the growth of dense anhydrous minerals (garnet and eclogite), drive aqueous fluids into the mantle wedge and initiate the generation of calc-alkaline magmas (e.g. Grove et al., 2006 and references therein).

In Fig. 12, it is straightforward to observe a concentration of earthquake activity at the head of the Argolic Gulf, as well as a rough N330° alignment of hypocentres between the head of the Argolic and the Gulf of Corinth. These features are pointed to by an up-arrow in Fig. 13 and roughly coincide with the inflection of the slab. It is also straightforward to observe 6 or 7 hypocentres at depths of approx. 120km beneath the Argolic Gulf and Plain. It is very plausible that these correspond to mislocated events. Note, though, that there are only eight 'outlying' hypocentres in Fig. 13 and of those six are observed at the same area and depth. It stands to reason that this may not be a mere coincidence, given also the column of reduced resistivity observed at depths between 140km and 60km just under and within the inflection of the slab (see below).

Very important observations can be made with respect to the electrical resistivity structure (Fig. 13). Within the slab, the inflection is associated with resistivity of the order of 700–900 Ωm embedded in a domain with resistivity higher than 1100 Ωm. The occurrence of earthquakes along this range of depths (60 – 80 km) implies dehydration embrittlement of the subducting metabasite crust: therefore, the drop in resistivity may, partially at least, be attributed to the presence of aqueous fluids and/or partial melting in the slab. This process may also drive water into the mantle wedge and be responsible for the relatively low resistivity observed in the lower crust of the overriding (Aegean) plate, directly above the inflection. It also stands to reason that if the "outlying" earthquakes beneath the inflection are not mislocated, their association with relatively low resistivity may imply that this region is associated with deep rooted and by all probability significant geodynamic processes. Although this is a very interesting problem, it shall not be pursued herein as it transcends the scope of this work.

Another important observation is the domain of relatively low resistivity (100 – 500 Ωm) observed in the mantle wedge and the lower crust of the Aegean plate, immediately above the slab and to the east of the inflection. Significantly enough, this is clearly collocated with the thinning of the Aegean plate beneath the Argolic Gulf and Plain, which can be attributed to tectonics (extension) as well as sub-lithospheric erosion due to magmatic underplating beneath the area of the volcanic arc. At any rate, the thinning extends at least between 37°N and 38.4°N and commences right beneath the east coast of the Peloponnesus/ west flank of the Argolic Plain, far from the volcanic arc (see Fig. 5 of Sachpazi et al.,

2005); its coincidence with these large scale extensional structures indicates that tectonics should be the primary genitor. Beneath this region, the slab is located at depths of the order of 60–80km and has entered the blueschist (amphibolitic) metamorphic facies by which aqueous fluids are driven into the mantle wedge due to chlorite dehydration; this process is thought to cause significant reduction of resistivity (e.g. Manthilake et al., 2016; references therein). Accordingly, we consider plausible that mantle wedge hydration, combined with decompression due to the extensional thinning of the Aegean plate generate magma in the mantle wedge that not only depresses the resistivity, but also ascends to the Aegean crust along the active extensional and transtensional fault network, eventually solidifying in the upper crust and generating the deep magnetic anomaly sources (plutons) detected herein.

A final noteworthy observation is that the range of resistivities shown in Fig. 13 for the lower Aegean crust, are compatible with analogous results of magnetotelluric modeling by Pham et al. (2000), who have estimated an average of 400 Ωm beneath the area 22.1°E – 22.2°E and 38.0°N – 38.1°N. What these authors did not have incentive to observe at that time, is that their study area is almost directly located on the (imaginary) north-westward extension of the Argolic Gulf; they also could not have known that it is located directly above the thinning of the Aegean plate crust, as this was mapped by Sachpazi et al., (2005). This implies that the lower crustal resistivity estimated by Pham et al., (2000) is likely to have been generated by processes similar to those operating beneath the Argolic Gulf and Plain. If true, this would imply that for the most part, the depression of lower crustal resistivity beneath the entire northeastern Peloponnesus is thermally induced. In turn, this would be consistent with a mechanically weak lower Aegean crust, as demanded by influential models of the inception and evolution of the Corinth Rift (e.g. Armijo et al., 2996; Westaway, 2002).

5.3 Intermediate and Shallow Magnetic Anomaly Sources

The origin of anomalies generated at depths shallower than 3km is occasionally not straightforward to assess. This lies with the fact that in some cases intrusion may take place in areas adjacent to ophiolitic masses, or even through them. Two of these cases are the Epidavros Anomaly (*EA*) which is partially fused with the Epidavros Ophiolite (*EO*) anomaly and the Radon anomaly (*Rd*) which is fused with the Radon Ophiolite (*RdO*) anomaly. In the former case, the source is deeply rooted and evidently offset to the south with respect to the EO outcrop (compare Fig. 9 and Fig. 10). Given the characteristics of north Argolid ophiolites and by analogy to the *Her-HdG-HdS* deep-source anomaly, the *EA* is more likely to be generated by a pluton. The upper parts of the intrusion may have risen to depths comparable to the deeper roots of the ophiolites (ca. 2 km), or even shallower penetrating right through them. In any case, there is no direct evidence of an intrusion through the ophiolitic formation in the area of Epidavros and the separation of anomalies generated by intrusive and ophiolitic sources would not be possible without additional structural information. It can easily be ascertained that the Radon anomaly first appears at a depth of approx. 3 km, where ophiolites are unlikely to exist, and has an amplitude of 20 nT. The main part of the anomaly is generated by sources buried between 3 and 2 km (amplitude up to 160 nT in Fig. 10). Moreover, the anomaly is located on a W-E trans-tensional faulting structure terminating at the strait between Troezenia and Poros Island (Fig. 11 and Section 5.4). Thus, one cannot rule out that the deeper part of the Radon anomaly (*Rd*) is igneous of origin. Nevertheless, the near coincidence of the anomaly and the ophiolitic outcrop does not allow conclusions to be drawn with confidence. In a last comment, it should be noted that the Pausanias submarine volcano (*Ps* in Fig. 11) appears to be a rather minor feature, as its magnetic signature is certainly localized with a source depth apparently less than 2 km.

Turning, finally, our attention to the shallow (< 2km) sources and with particular reference to the southern Argolid, we note that the W-E configuration of the (outcropping or buried) ophiolitic sources may also be explained in terms of tectonics. Faulting processes rupture magnetized rock formations, "shearing" the local total intensity field and producing lateral gradients. Moreover, they initiate secondary processes that destroy magnetic susceptibility and remanent magnetization by facilitating water infiltration and chemical alteration, thereby creating "ridges" and "valleys" in the total intensity field. The location of the fault would, then, be indicated by the "valley" structures. Also, the interfaces between magnetic and non-magnetic geological formations brought in contact by tectonic action are evident by abrupt lateral changes in the intensity of the magnetic field. As a consequence, tectonic processes may result in elongate discontinuities (lineaments) in the anomalous magnetic field, which should be collocated and correlated with fault zones. It is not difficult to see that this may well be the case for the anomalies associated with the W-E oriented *HlO–Fournoi* and *RdO* ophiolitic formations, which are flanked by W-E oriented faults (Fig. 11 and Fig. 14). The *HlO–Fournoi* ophiolites in particular, appear to sit directly on the horst of the Mt Adheres range and are thus tectonically delimited and completely separated from the deep-seated *Her-HdG-HdS* sources. In support of this inference, it is worth pointing out that anomalies associated with the *HlO–Fournoi* formation (Fig. 11) are conspicuously absent from Fig. 10 (anomalies generated by sources buried at depths greater than 2 km).

5.4 Deformation and Crustal Magmatism in Argolis Peninsula: A Model

An interesting aspect of our results is that active faulting with non-trivial W-E lateral heave has been deduced by formal inversion of earthquake focal mechanisms and is expected to operate between the Argolic and east Saronic gulfs, with particular reference to the central and southern Argolid (Argolis Peninsula). The possibility of lateral-heave faulting in that area has not gone unnoticed in previous research. For instance, Van Andel et al. (1993) postulated the existence of two W-E left-lateral faults bracketing the north and south flanks of the Didymon – Adheres ranges and forming the homonymous horst. Given the evidence available to them at that time this fault kinematics was reasonable inference. However, our work has demonstrated not only that W-E faults with a significant horizontal slip component are expected in the area, but that they actually are *right-lateral*. This presents a small problem in that the peninsula must shift due east along dextral faults and not along sinistral faults as would intuitively be expected.

The issue can be resolved if the area of Argolis peninsula is taken to comprise a crustal block undergoing internal deformation modulated by the synthetic R-shear faulting direction, as schematically depicted in Fig. 14. According to this view, the Argolis block is approximately delimited to the NW by a putative regional SW-NE shear fault zone extending along the southeastern flank of Mt Arachnaeon through to Nea Epidavros, and to the SE by the regional fault zone that forms the (graben of) Hydra Strait and is marked as HdF (Hydra Fault) in Fig. 14. In this way the southernmost areas of Hermionis and Hydra Gulf are relatively stationary, bounded to the east by the HdF system. However, the central and south Peninsula can slide due east by right-lateral faulting, in a configuration comprising three major blocks, of which the central (Didymon – Adheres block) is moving relatively faster than the northern (Mavrovouni block) and southern (Hermionis block). The locations of the W-E faults delimiting the Didymon – Adheres block are approximately as postulated by Van Andel et al., (1993), but have been adjusted with respect to the W-E intrusive activity discovered herein. It is also conceivable that the two major blocks comprise ensembles of minor

blocks bounded by secondary W-E lateral-heave faulting. Both major and secondary faults may be reactivated structures older than the inception of the Corinth Rift, or structures inherited from the earlier stages of Corinth Rift formation (Late Pliocene).

This model is consistent with the differences in the configuration of major normal faulting at the west and east coasts of the peninsula, namely the NW-SE south-westerly dipping faults of the Argolic coast vs. the WNW-ESE north-easterly dipping faults of the Saronic coast. It is rather easy to see how any consequent strain differential due to disparity in the extension directions (and rates) of the Argolic and Saronic gulfs can be accommodated by the right-lateral drift. The model is also consistent with the localization of intrusive activity in certain zones of more intense W-E deformation, specifically: (a) Along the Hermionis – Hydra Gulf – Hydra Strait – Cape Skillaion line, just off the southern boundary faults of the Didymon – Adheres block. (b) Along the Kalloni – Poros line at the eastern end of the boundary separating the Didymon – Adheres and Mavrovouni blocks, and, (c) along the Palaea Epidavros – Methana line coincidentally with the northern boundary of the Mavrovouni block. Finally, the model is consistent with the anisotropic W-E geographical configuration and geomorphological characteristics of the central and southern Argolis peninsula (also see Vassilopoulou, 1999, 2010). In order to exemplify this point, Fig. 14 is underlain by a shaded relief image of the topography, lit from the north.

As a concluding general comment, we note that we have found evidence of extensive, hitherto unknown and largely unsuspected syn-rift plutonic magmatism beneath the Argolid, apparently related to the Hellenic Subduction and Volcanic Arc, as well as to rifting in the Corinth Rift system. This type of large scale intrusive activity indicates a link (interaction) between deep-seated processes related to the local characteristics of the subducting slab and the deformation of the southwestwardly moving crust of the Aegean forearc. The mechanism generating the local deformation pattern postulated for Argolis peninsula is certainly part of these processes. The analysis and identification of such interactions will not be pursued herein; they will be revisited in follow-up work with the aid of additional multi-parametric observational evidence.

Acknowledgements

We are indebted to Dr V. Sakkas and Dr E. Lagios (Department of Geology and Geo-environment, National and Kapodestrian University of Athens), for providing the raw output of the inversion of the magnetotelluric cross-section presented in Galanopoulos et al., (2005). We sincerely appreciate several astute and punctual comments by Dr D. J. W. Piper of the Geological Survey of Canada. We also acknowledge several insightful discussions with Dr Haralambos Kranis (Department of Geology and Geo-environment, National and Kapodestrian University of Athens).

References

Amante, C. and Eakins, B.W., 2009. ETOPO1 1 Arc-Minute Global Relief Model: Procedures, Data Sources and Analysis. NOAA Technical Memorandum NESDIS NGDC-24. National Geophysical Data Center, NOAA. doi:10.7289/V5C8276M; last accessed December 2016).

Armijo, R., Meyer, B., King, G., Rigo, A. and Papanastassiou, D., 1996. Quaternary evolution of the Corinth Rift and its implications for the late Cenozoic evolution of the Aegean, Geophys. J. Int.,

126, 11–53.

Avallone, A., Briole, P., Agatza-Balodimou A-M., Billiris, H., Charadea, O., Mitsakaki, C., Nercessian, A., Papazissi, K., Paradissis, D. and Veis, G., 2004. Analysis of eleven years of deformation measured by GPS in the Corinth Rift Laboratory area. Comptes Rendus Geoscience, 336, 301–311; doi:10.1016/j.crte.2003.12.007

Basili, R., Kastelic, V., Demircioglu, M. B., Garcia Moreno, D., Nemser, E. S., Petricca, P., Sboras, S. P., Besana-Ostman, G. M., Cabral, J., Camelbeeck, T., Caputo, R., Danciu L., Domac, H., Fonseca, J., García-Mayordomo, J., Giardini, D., Glavatovic, B., Gulen, L., Ince, Y., Pavlides, S., Sesetyan, K., Tarabusi, G., Tiberti, M.M., Utkucu, M., Valensise, G., Vanneste, K., Vilanova, S., Wössner J., 2013. The European Database of Seismogenic Faults (EDSF) compiled in the framework of the Project SHARE. *http://diss.rm.ingv.it/share-edsf/*, doi: 10.6092/INGV.IT-SHARE-EDSF (last accessed December 2016).

Bhattacharyya, B.K. and Leu, L.K., 1975. Spectral analysis of gravity and magnetic anomalies due to two-dimensional structures, Geophysics 40, 993–1013.

Billiris H., Paradissis D., Veis G., England P., Featherstone W., Parsons B., Cross P., Rands P., Rayson M., Sellers P., Ashkenazi V., Davison M., Jackson J., Ambrseys N., 1991. Geodetic determination of tectonic deformation in central Greece from 1900 to 1988, Nature, 350, 124-129.

Blakely, R.J., 1995. Potential Theory in Gravity and Magnetic Applications, Cambridge University Press.

Bondar, I. and D. Storchak, 2011, Improved location procedures at the International Seismological Centre, Geophys. J. Int., 186, 1220-1244; doi: 10.1111/j.1365-246X.2011.05107.x.

Briole P., Rigo A., Lyon-Caen H., Ruegg J.C., Papazissi K., Mitsakaki C., Balodimou A., Veis G., Hatzfeldand D., and Deschamps A., 2000. Active deformation of the Corinth Rift, Greece: results from repeated Global Positioning System surveys between 1990 and 1995. J. Geophys. Res., 105, 25605–25625.

Chailas S., Tzanis A., Kranis H. and Karmis P., 2010. Compilation of a unified and homogeneous aeromagnetic map of the Greek Mainland. Bull. Geol. Soc. Greece, 43 (4), 1919-1929; available at http://www.geosociety.gr/images/arxeio-teuxwn/GSG_XLIII_4.pdf (last accessed December 2016).

Clarke, P. J., Davies, R. R., England, P. C., Parsons, B., Billiris, H., Paradissis, D., Veis, G., Cross, P. A., Denys, P. H., Ashkenazi, V., Bingley, R., Kahle, H.-G., Muller, M.-V. and Briole, P., 1998. Crustal strain in central Greece from repeated GPS measurements in the interval 1989 – 1997, Geophys. J. Int., 135 (1), 195 – 214.

D'Alessandro A., Papanastasiou D. and Baskoutas I., 2011. Hellenic Unified Seismological Network: an evaluation of its performance through SNES method, Geophys. J. Int., 185 (3), 1417–1430; doi: 10.1111/j.1365-246X.2011.05018.x

Daubechies, I., 1992. Ten lectures on Wavelets, CBMS Regional Conference Series in Applied Mathematics, SIAM, Philadelphia, PA.

DeMartini, P.M., Pantosti, D., Palyvos, N., Lemeille, F., McNeill, L., and Collier, R., 2004. Slip rates of the Aigion and Eliki faults from uplifted marine terraces, Corinth Gulf, Greece: Comptes Rendus Geoscience, v. 336, p. 325– 334, doi: 10.1016/j.crte.2003.12.006.

Dietrich, V. and Gaitanakis, P., 1995. Geological Map of Methana Peninsula (Greece). ETH Zürich, Switzerland.

Dotsika, E. Poutoukis, D.and Raco, B., 2010. Fluid geochemistry of the Methana Peninsula and Loutraki geothermal area, Greece. Journal of Geochemical Exploration, 104, 97-104; doi:

10.1016/j.gexplo.2010.01.001.

Doutsos, T. and Piper, D. J. W. 1990. Listric faulting, sedimentation, and morphological evolution of the Quaternary eastern Corinth rift, Greece: first stages of continental rifting. Geological Society of America Bulletin, 102, 812–829

Drakatos G, Karastathis V, Makris J, Papoulia J, Stavrakakis G., 2005. 3D crustal structure in the neotectonic basin of the Gulf of Saronikos (Greece), Tectonophysics, 400, 55-65.

Efstathiou, A., 2011. Volcanism and geothermy at the Argolis Peninsula (East Peloponnesus, Greece). MSc Thesis, Faculty of Geology, National and Kapodistrian University of Athens.

Flotté , N., S, D., Miller, C. and Tensi, J. 2005. Along strike changes in the structural evolution over a brittle detachment fault: example of the Pleistocene Corinth–Patras rift (Greece). Tectonophysics, 403, 77– 94.

Francalanci, L, Vougioukalakis, G.E, Perini, G. and Manetti, P., 2005. A West-East Traverse along the magmatism of the south Aegean volcanic arc in the light of volcanological, chemical and isotope data: In M. Fytikas and G. Vougioukalakis (eds), The South Aegean Volcanic Arc, Present Knowledge and future perspectives, Elsevier, 65-111.

Gaitanakis P. and Photiades A.D., 1989. The ophiolitic units of the Argolid (Peloponnese, Greece), Bull. Geol. Soc. Greece, 23 (1), 363-380 (in Greek with French abstract).

Gaitanakis, P. and Photiades, A., 1993. New data on the geology of Southern Argolid, Bull. Geol. Soc. Greece, vol. 28 (1), 247-267 (in Greek with English abstract).

Gaitanakis, P. and Photiades, A.D., 1991. Geological structure of SW Argolid, Bull. Geol. Soc. Greece, vol. 25 (1), 319-338 (in Greek with French abstract).

Galanopoulos D., Sakkas V., Kosmatos D. and Lagios E., 2005. Geoelectric investigation of the Hellenic subduction zone using long period magnetotelluric data. Tectonophysics 409, 73–84.

Goldsworthy, M. and Jackson, J., 2001. Migration of activity within normal fault systems: examples from the Quaternary of mainland Greece, Journal of Structural Geology, 23, 489–506.

Grove, T.L., Chatterjee, N., Parman, S.W. and Médard, E., 2006. The influence of H_2O on mantle wedge melting, Earth and Planetary Science Letters, 29, 74-89; doi: 10.1016/j.epsl.2006.06.043.

Hardebeck, J. L. and Hauksson, E., 2001. Stress orientations obtained from Earthquake focal mechanisms: What are appropriate uncertainty estimates?, Bull. Seismol. Soc. Am., 91, 250–262; doi:10.1785/0120000032, 2001.

Hardebeck, J. L., and Michael, A.J., 2006. Damped regional-scale stress inversions: Methodology and examples for southern California and the Coalinga aftershock sequence, J. Geophys. Res. 111, no. B11, B11310; doi: 10.1029/2005JB004144.

Hatzfeld, D., Besnard, M., Makropoulos, K. and Hatzidimitriou, P., 1993. Microearthquake seismicity and fault plane solutions in the southern Aegean and its geodynamic implications. Geophys. J. Int., 115, 799-818.

Hatzfeld, D., Pedotti, G., Hatzidimitriou, P., Panagiotopoulos, D., Scordilis, M., Drakopoulos, I., Makropoulos, K., Delibasis, N., Latousakis, I., Baskoutas, J. and Frogneux, M., 1989. The Hellenic subduction beneath the Peloponnesus: first results of a microearthquake study, Earth and Planetary Science Letters, 93, 283-291.

Kahle, H-G., Cocard, M., Yannick, P., Geiger, A., Reilinger, R., Barka, A. and Veis, G., 2000. GPS-derived strain field within the boundary of the Eurasian, African and Arabian Plates. J. Geoph. Res., 105, 23353-23370.

Kaplanis, A., Koukouvelas, I., Xypolias, P. and Kokkalas, S., 2013. Kinematics and Ophiolite obduction in the Gerania and Helicon Mountains, central Greece, Tectonophysics 595–596, 215–

234; http://dx.doi.org/10.1016/j.tecto.2012.07.014

Kiratzi A. and Louvari E., (2003), Focal mechanisms of shallow earthquakes in the Aegean Sea and the surrounding lands determined by waveform modelling: a new database. Journal of Geodynamics, 36, 251–274.

Konstantinou, K. I., Melis, N. S. and Boukouras, K., 2010. Routine regional moment tensor inversion for earthquakes in the Greek region: The National Observatory of Athens (NOA) database (2001-2006), Seismol. Res. Lett., 81, 750–760, doi:10.1785/gssrl.81.5.738.

Kotopouli, C.,N., Pe-Piper, G. and Piper, D.J.W, 2000. Petrology and evolution of the Hercynian Pieria Granitoid Complex (Thessaly, Greece): paleogeographic and geodynamic implications, Lithos, 50, 137-152; DOI: http://dx.doi.org/10.1016/S0024-4937(99)00054-7.

Kranis, H.D. 1999. Neotectonic activity of fault zones in Lokris, central-eastern mainland Greece, Ph.D. Thesis, Faculty of Geology, National and Kapodistrian University of Athens, (GAIA publ. No 10), 234. pp.

Leeder, M.R., Mark, D.F., Gawthorpe, R.L., Kranis, H. , Loveless, S., Pedentchouk, N., Skourtsos, E., Turner, J., Andrews, J.E. and Stamatakis, M., 2012. A "Great Deepening": Chronology of rift climax, Corinth rift, Greece, Geology, 40 (11), 999-1002; doi:10.1130/G33360.1

Manthilake, G., Bolfan-Casanova, N. Novella, D., Mookherjee, M. and Andrault, D., 2016. Dehydration of chlorite explains anomalously high electrical conductivity in the mantle wedges, Science Advances, 2 (5), e1501631; doi: 10.1126/sciadv.1501631.

Martínez-Garzón, P., Kwiatek, G, Ickrath, M. and Bohnhoff, M, 2014. MSATSI: A MATLAB Package for Stress Inversion Combining Solid Classic Methodology, a New Simplified User-Handling and a Visualization Tool, Seismol. Res. Let., 85 (4), doi: 10.1785/0220130189.

McClusky, S.C., Balassanian, S., Barka, A., Demir, C., Ergintav, S., Georgiev, I., Gurkan, O., Hamburger, M., Hurst, K., Kahle, H., Kastens, K., Kekelidze, G., King, R., Kotzev, V., Lenk, O., Mahmoud, S., Mishin, A., Nadariya, M., Ouzounis, A., Paradissis, D., Peter, Y., Prilepin, M., Reilinger, R., Sanli, I., Seeger, H., Tealeb, A., Toksoz, M.N., and Veis, G., 2000, Global positioning system constraints on plate kinematics and dynamics in the eastern Mediterranean and Caucasus: Journal of Geophysical Research, 105(B3), 5695–5719.

McNeill, L.C., Cotterill, C.J., Henstock, T.J., Bull, J.M., Stefatos, A., Collier, R.E.Li., Papatheodorou, G., Ferentinos, G., Hicks, S.E., 2005. Active faulting within the offshore western Gulf of Corinth, Greece: implications for models of continental rift deformation. Geology, 33, 241–244, doi: 10.1130/G21127.1.

Michael, A. J., 1991. Spatial variations in stress within the 1987 Whittier Narrows, California, aftershock sequence: New techniques and results. J. Geophys. Res., 96, 6303–6319, 1991.

Michael, A.J., 1984. Determination of Stress from Slip Data: Faults and Folds, *J. Geophys. Res.*, 89, 11517-11526.

Michael, A.J., 1987. Use of Focal Mechanisms to Determine Stress: A Control Study, *J. Geophys. Res.*, 92, 357-368.

Mitropoulos, P., 1987. Primary allanite in andesitic rocks from the Poros Volcano, Greece, Mineralogical Magazine, 51, 601-604.

Papadeas, G., 1989. Geological map of Attica, Institute of Geological and Mineral Exploration (IGME), Athens, Greece.

Papanikolaou D., Lykousis V., Chronis G. and Pavlakis, P., 1988. A comparative study of neotectonic basins a cross the Hellenic Arc: the Messiniakos, Argolikos, Saronikos and Southern Evoikos Gulfs. Basin Research 1, 167-176.

Papanikolaou, D. and Lozios, S., 1990. Comparative neotectonic structure of high (Korinthia-Beotia) and low rate (Attica-Cyclades) activity, Bull. Geol. Soc. Greece 26, 47-66 (in Greek with English abstract); available at http://geolib.geo.auth.gr/digeo/index.php/bgsg/article/view/809/761 (last accessed December 2016).

Papazachos, B.C., Karakostas, V.E., Papazachos, C.B. and Scordilis, E.M., 2000. The geometry of the Wadati–Benioff zone and lithospheric kinematics in the Hellenic arc, Tectonophysics, 319(4), 275–300.

Pawlowski, R. S., and R. O. Hansen, 1990, Gravity anomaly separation by Wiener filtering: Geophysics,55, 539, doi:10.1190/1.1442865.

Pe-Piper, G., 2000. Origin of S-type granites coeval with I-type granites in the Hellenic subduction system, Miocene of Naxos, Greece, European Journal of Mineralogy, 12 (4), 859 – 875; DOI: 10.1127/ejm/12/4/0859.

Pe-Piper, G. and Piper, D.J.W., 2002. The Igneous Rocks of Greece: anatomy of an orogen. Bornträger, Berlin.

Pe-Piper, G. and Piper, D.J.W., 2013. The effect of changing regional tectonics on an arc volcano: Methana, Greece, J volc. geotherm. Res, 260, 146-163; DOI: 10.1016/j.jvolgeores.2013.05.011

Peter, Y., Kahle, H., Cocard, M., Veis, G., Felekis, S. and Paradissis, D., 1998. Establishment of a continuous GPS network across the Kephalonia Fault Zone, Ionian islands, Greece, Tectonophysics, 294(3-4), 253–260.

Pham, V.N., Bernard, P., Boyer, D., Chouliaras, G., Le Mouël, J.L and Stavrakakis, G.N, 2000. Electrical conductivity and crustal structure beneath the central Hellenides around the Gulf of Corinth (Greece) and their relationship with the seismotectonics, Geophys. J. Int., 142, 948-969.

Photiades, A.D. and Keay, S., 2000. Mid-Late Jurassic granodiorite basement in southern Argolis Peninsula (Greece): Tectonostratigraphic implications, in Panayides, I, Xenophontos, C. and Malpas, J., (eds), Proceedings of the 3rd International Conference on the Geology of the Eastern Mediterranean, Geol. Surv. Dpt. Cyprus, pp. 233-239.

Ritsema, A., 1974. The earthquake mechanics of the Balkan region. R. Netherl. Meteorol. Inst., De Bilt, Sci. Rep 4–74.

Sachpazi, M., Clement, C., Laigle, M., Hirn, A. and Roussos, N. 2003. Rift structure, evolution, and earthquakes in the Gulf of Corinth, from reflection seismic images.. Earth Plan. Sci. Let., 216, 243-257.

Sachpazi, M., Galvé, A., Laigle, M., Hirn, A., Sokos, E., Serpetsidaki, A., Marthelot, J.-M., Pi Alperin, J.M., Zelt, B., and Taylor, B., 2007. Moho topography under central Greece and its compensation by Pn time-terms for the accurate location of hypocentres: The example of the Gulf of Corinth 1995 Aigion earthquake, Tectonophysics 440, 53–65; doi: 10.1016/j.tecto.2007.01.009

Sachpazi, M., Laigle, M., Charalampakis, M., Diaz, J., Kissling, E., Gesret, A., Becel, A., Flueh, E., Miles, P. and Hirn, A., 2016. Segmented Hellenic slab rollback driving Aegean deformation and seismicity, Geophys. Res. Lett., 43, 651–658, doi: 10.1002/2015GL066818.

Skourtsos, E. and Kranis, H., 2009. Structure and evolution of the western Corinth Rift, through new field data from the Northern Peloponnesus, in Ring, U. and Wernicke, B. (eds), Extending a Continent: Architecture, Rheology and Heat Budget. The Geological Society, London, Special Publications, 321, 119–138; doi: 10.1144/SP321.6

Smet, I., 2014. Spatial and temporal petrological-geochemical variations in the volcanic rocks of the Saronic Gulf (West Aegean arc, Greece): Influence of local geodynamic parameters on magma genesis. PhD thesis, Ghent University, Belgium, 349pp.

Spector, A. and Grant, F.S., 1970. Statistical models for interpreting aeromagnetic data, Geophysics, 35 (2), 294-302.

Sperner, B., Müller, B., Heidbach, O., Delvaux, D., Reinecker, J. and Fuchs, K., 2003. Tectonic stress in the Earth's crust: advances in the World Stress Map project. - In: Nieuwland, D.A. (ed.): New insights in structural interpretation and modelling, Geol. Soc. Lond. Spec. Publ., 212, 101-116.

Stefatos, A., Papatheodorou, G., Ferentinos, G., Leeder, M. and Collier, R. 2002. Seismic reflection imaging of active offshore faults in the Gulf of Corinth: their seismotectonic significance. Basin Research, 14, 439-542.

Suckale, J., Rondenay, S., Sachpazi, M., Charalampakis, M., Hosa, A. and Royden, L.H., 2009. High-resolution seismic imaging of the western Hellenic subduction zone using teleseismic scattered waves. Geophys. J. Int., 178, 775–791; doi: 10.1111/j.1365-246X.2009.04170.x.

Taktikos, S., 2001. Heat flow – Underground temperatures of Greece; set of two volumes and 12 maps, Institute of Geological and Mineral Exploration (IGME), Athens, Greece (in Greek).

Tselentis, G-A., 1991. An attempt to define Curie point depths in Greece from aeromagnetic and heat flow data, Pure and Applied Gephysics, 136 (1), 87-101.

Tzanis, A., Kranis, H. and Chailas, S., 2010. An investigation of the active tectonics in central-eastern mainland Greece, with imaging and decomposition of topographic and aeromagnetic data. J. Geodyn., 49, 55 – 67; doi:10.1016/j.jog.2009.09.042.

Van Andel, T.H., Perissoratis, C. and Rondoyanni, T., 1993. Quaternary tectonics of the Argolikos Gulf and adjacent basins, Greece, Journal of the Geological Society, London, 150, 529-539.

Vassilopoulou S., 1999. Geodynamics of the Argolis Peninsula with G.I.S development and use of Remote Sensing Data. PhD Thesis, Faculty of Geology, National and Kapodistrian University of Athens (in Greek).

Vassilopoulou S., 2010. Morphotectonic analysis of Southern Argolis Peninsula (Greece) based on ground and satellite data by GIS development. Bull. Geol. Soc. Greece, 43 (1), 516-525; available at http://www.geosociety.gr/images/arxeio-teuxwn/GSG_XLIII_1.pdf (last accessed December 2016).

Wessel, P., Smith, W.H.F., Scharroo, R., Luis, J.F. and Wobbe, F., 2013. Generic Mapping Tools: Improved version released, EOS Trans. AGU, 94, 409-410; doi: 10.1002/2013EO450001.

Westaway, R., 2002. The Quaternary evolution of the Gulf of Corinth, central Greece: coupling between surface processes and flow in the lower continental crust. Tectonophysics, 348, 269–318.

Xia, J., Sprowl, D.R. and Adkins-Heljeson, D., 1993. Correction of topographic distortions in potential-field data: A fast and accurate approach; Geophysics, 58(4), 515-523.

Zoback, M.D. and Zoback, M.L., 1991. Tectonic stress field of North America and relative plate motions, in Slemmons, D.B., Engdahl, E.R., Zoback, M.D. and Blackwell, D.D. (eds.), Neotectonics of North America, 339-366.

Zoback, M.L. and Zoback, M.D., 1989. Tectonic stress field of the conterminous United States, Mem. Geol. Soc. Am., 172, 523-539.

APPENDIX A – Wavelet filters for effective separation of potential field anomalies

Magnetic anomaly separation directly relevant to the depth of the sources can be based on a wavenumber domain Wiener filtering approach, as for instance in the scheme proposed by Pawlowski and Hansen (1990). This method uses the ensemble power spectrum $P_r(k)$ to represent the signal power and defines one-dimensional zero-phase Wiener filters of the form

$$G_{PH}(k) = \frac{A \cdot k^2 \cdot e^{-2kZ_1}}{P_r(k)}, \qquad \text{(A.1)}$$

where the nominator comprises the response of a depth-limited source ensemble whose ceiling is buried at a depth of Z_1 km, as expressed by Spector and Grant (1970). The one-dimensional filters can be subsequently mapped onto zero-phase matrix (2-D) filters and applied to the data in the Fourier domain. A similar approach implements the response of depth-limited ensembles whose ceilings and floors are buried at depths $Z_1 > Z_2$ respectively. Blakely (1995) has shown that this is

$$H(k) = Be^{-2kZ_2}\left(1 - e^{-k(Z_1 - Z_2)}\right)^2,$$

so that the corresponding Wiener filter would be

$$G_B(k) = \frac{Be^{-2kZ_2}\left(1 - e^{-k(Z_1 - Z_2)}\right)^2}{P_r(k)} \qquad \text{(A.2)}$$

Clearly, G_{PH} and G_B comprise classes of band-pass filters designed to isolate the response of depth-limited ensembles on the basis of information extracted from the radially averaged power spectrum. These approaches have a cardinal advantage in that they guide the separation of anomalies on the basis of structural information directly recoverable from the data. However, they are not effective as can be easily demonstrated.

In the scenario of Fig. A1a, the analysis seeks to separate an ensemble of sources (target) known to be buried between Z_1 = 3.8km and Z_2 = 1.8km, when the Nyquist wavenumber is 4π cycles/km, meaning that the input data have a grid spacing of 0.25km as with the data treated herein (Section 4). Logic dictates that the target ensemble would be delimited by the wavenumber corresponding to the peak of a Spector and Grant (S&G) response computed for Z_1 = 3.8km, which is k_1 = 0.2592 cycles/km, and the wavenumber corresponding to the peak of a S&G response computed for Z_2 = 1.8km, which is k_2 = 0.5576 cycles/km: the argument assumes that the target ensemble is succeeded by a depth-limited concentration of sources but this is inconsequential to the analysis. The peak wavenumber of the Blakely response is k_0 = 0.3762 cycles/km, which is neatly situated at approximately midways between k_1 and k_2. Clearly, $G_{PH}(k_1)$ and $G_{PH}(k_2)$ are neither efficient nor effective: Due to their bell-shaped form and blunt roll-off, they significantly attenuate proper spectral content of the target ensemble while assimilating shorter than k_1 or longer than k_2 spectral content, that is from depths below the floor or above the ceiling of the ensemble. Equally clearly, $G_B(Z_1,\ Z_2)$ fares much better, although not very well. To begin with, it attenuates some spectral content of the target ensemble: the amplitudes at wavenumbers k_1 and k_2 are reduced by 12% and 16% respectively, which it certainly not excessive but also not desirable. Conversely, it admits information from spectral content outside of the target ensemble: 77% and 80% of the spectral components at k = 0.2238 < k_1 and k = 0.604 > k_2 are admitted, while the low roll-off rates ensure that a significant amount of outside information will be filtered-in. These examples make evident that efficient recovery of the spectral signatures of depth-limited sources requires filters with flat as possible pass bands for $k \in [k_1, k_2]$ and sharp as possible

roll-off bands for $k <\notin [k_1, k_2]$. The problem can be addressed with conventional IIR or FIR filters. These, however, are complex in the Fourier domain and have to be applied in the forward and reverse spatial sense in order to avoid translations in the location of anomalies. This is not a problem in itself but such filters are also associated with ripple structure whose suppression is linked to the width of the pass band, the roll-off rate and the magnitude of phase shifts, particularly when the pass band is narrow and/or squeezed at the short wavenumber realm: their design is not always straightforward or optimal.

In response to the difficulties described above, herein, we introduce a set of filters with all the desirable characteristics. Specifically, these filters are a) *real* in the Fourier plane (no phase shifts), b) have perfectly flat pass bands (no ripples), c) are automatically localizable with respect to any interval $[k_1, k_2]$, and, d) exhibit optimally sharp roll-off bands so as to suppress all information outside the span of the target ensemble. The filters will be described at an elementary (introductory) level, with due rigour reserved for a follow-up, more specialized presentation.

Consider a smooth and *admissible* profile $W(r)$ compactly supported on $[-2, -1/2] \cup [1/2, 2]$. This allows for particularly efficient localization and has been used for the development of *Meyer* wavelets. W is a Meyer Window (MW) when it has the form, (see Daubechies, 1992, pp. 115-120),

$$W(r) = \begin{cases} \cos\left[\frac{\pi}{2} w(5-6r)\right] & 2/3 \le r \le 5/6 \\ 1 & 5/6 \le r \le 4/3 \\ \cos\left[\frac{\pi}{2} w(3r-4)\right] & 4/3 \le r \le 5/3 \\ 0 & otherwise \end{cases}, \tag{A.3}$$

with $w(x)$ satisfying

$$w(x) = \begin{cases} 0 & x \le 0 \\ 1 & x \ge 1 \end{cases}, \qquad w(t) + w(1-x) = 1, \qquad x \in \mathbb{R}. \tag{A.4}$$

In order to obtain smooth W, it is necessary to use smoother $w(x)$. Common forms are the polynomials $w(x) = 3x^2 - 2x^3$ or $w(x) = 5x^3 - 5x^4 + x^5$ in [0, 1], such that $w \in C^1(\mathbb{R})$ and $w \in C^2(\mathbb{R})$ respectively. It is also possible to obtain arbitrarily smooth W when

$$w(x) \begin{cases} 0 & x \le 0 \\ \dfrac{s(x-1)}{s(x-1) + s(x)} & 0 < x < 1, \\ 1 & x \ge 1 \end{cases} \qquad s(x) = \exp\left(-\frac{1}{(1+x)^2} - \frac{1}{(1-x)^2} \right) \tag{A.5}$$

The Meyer Window can be localized and scaled with respect to a particular (target) wavenumber k_0 by letting $r = k/k_0$. In turn, k_0 can be specified manually, or be determined objectively on the basis of simulations of the radial spectrum with models obeying the Spector and Grant (1970), or Blakely (1995) formalisms.

An example of a one-dimensional MW profile constructed with the aid of the Blakely response is shown in Fig. A1a. As discussed above, the peak of the Blakely response corresponds to $k_0 = 0.3762$ cycles/km. The MW is automatically scaled around this particular k_0, as indicated with the thick solid line. In obvious contrast to the ensemble responses (or G_{PH} and G_B filters), the MW has a perfectly flat pass band and very sharp roll-off so that it will only admit information pertaining to a rather narrow band around k_0, and its output will *certainly not* be contaminated by irrelevant contributions from deeper or shallower sources. Nevertheless, it is equally obvious that in this case, the pass band of the

MW does not span the entire [k_1, k_2] interval: it is certainly more localized. Conversely, there may be instances in which the desired pass band is narrow enough for the window to transcend [k_1, k_2] so as to admit unwanted information.

Due to the limitations state above, the MW window will not be used in the present analysis; rather, it was presented as an intermediary by which to introduce a more useful construct that remedies its limitations while retaining its advantages. This construct, henceforth to be dubbed "*Extended Meyer Window*" or EMW, can be defined as follows:

$$F(r)=\begin{cases}\cos\left[\frac{\pi}{2}w(5-6r)\right], & \frac{2}{3}\le r\le\frac{5}{6} \;:\; r=\frac{5}{6}\frac{k}{k_1} \;\leftrightarrow\; k\le k_1\\ 1, & \frac{5}{6}<r<\frac{4}{3} \;:\; r=\frac{k}{\beta(k)} \;\leftrightarrow\; k_1<k<k_2\\ \cos\left[\frac{\pi}{2}w(3r-4)\right], & \frac{4}{3}\le r\le\frac{5}{3} \;:\; r=\frac{4}{3}\frac{k}{k_2} \;\leftrightarrow\; k_2\le k\\ 0 & \textit{otherwise}\end{cases} \tag{A.6}$$

As can be seen in Eq. (A.6), the terminus of the low-wavenumber cut-off is moved to k_1 by stretching (dilating or contracting) the pass band so that $r(k) \approx 5/6$ when $k \approx k_1$. Likewise, the origin of the high-wavenumber cut-off is moved to k_2 by stretching the pass band so that $r(k) \approx 4/3$ when $k \approx k_2$. The pass band is unity for all $r \in (5/6, 4/3)$ or, equivalently, $k \in (k_1, k_2)$. To achieve this (and compensate for stretching, a normalizing function $\beta(k)$ is necessary, such that

$$\frac{5}{6}\frac{k}{k_1}<\frac{k}{\beta(k)}<\frac{4}{3}\frac{k}{k_2} \quad\Rightarrow\quad \frac{6}{5}k_1>\beta(k)>\frac{3}{4}k_2\,;$$

$\beta(k)$ may be determined by interpolation, although in practice this is not required (see below). The EMW is *compactly supported* on [-2, -1/2] $\cup$ [1/2, 2] and can be shown to comprise an admissible profile: it is a filter and a *wavelet* at the same time. Formal proof of this claim is relatively easy and based on the same procedure proving that $W(r)$ is admissible (e.g. Daubechies, 1992). It will not be given herein for the sake of brevity but is reserved for a follow-up, more specialized and detailed presentation. Conversely, empirical (numerical) verification is rather straightforward: by taking the inverse Fourier transform $f(x)$ of *any* realization of $F(k)$, it is easy to determine that the *admissibility condition* $\Sigma_x f(x) = 0$, is *always* upheld.

An equivalent definition of the EMW, more useful for programming, is:

$$F(k)=\begin{cases}\cos\left[\frac{\pi}{2}w(5-5\frac{k}{k_1})\right], & \frac{2}{3}\le\frac{5}{6}\frac{k}{k_1}\le\frac{5}{6}\\ 1, & k_2<k<k_1\\ \cos\left[\frac{\pi}{2}w(4\frac{k}{k_2}-4)\right], & \frac{4}{3}\le\frac{4}{3}\frac{k}{k_2}\le\frac{5}{3}\\ 0, & \textit{otherwise}\end{cases} \tag{A.7}$$

Eq. (A.7) indicates that EMW filters can be converted to low-pass by letting

$$F_l(k)=\begin{cases}1 & k<k_2\\ \cos\left[\frac{\pi}{2}w(4\frac{k}{k_2}-4)\right] & \frac{4}{3}\le\frac{4}{3}\frac{k}{k_2}\le\frac{5}{3}\\ 0 & \textit{otherwise}\end{cases} \tag{A.8}$$

or to high pass by letting

$$F_h(r) = \begin{cases} \cos\left[\frac{\pi}{2} w(5 - 5\frac{k}{k_1})\right] & \frac{2}{3} \le \frac{5}{6}\frac{k}{k_1} \le \frac{5}{6} \\ 1 & k_1 < k \\ 0 & otherwise \end{cases} \qquad (A.9)$$

Fig. A1b illustrates an EMW band-pass profile appropriate for the analysis presented herein; it is designed to separate a depth-limited ensemble buried between Z_1 = 3.8km, (k_1 = 0.2592 cycles/km) and Z_2 = 1.8km (k_2 = 0.5576 cycles/km), where the wavenumbers correspond to the peaks of the respective depth-limited S&G responses. The EMW filter is perfectly flat for $k \in (k_1, k_2)$ and exhibits sharp roll-off, identical to that of the Meyer window; the left roll-off band terminates at exactly k_1 (low cut-off wavenumber) and the right roll-off band commences at exactly k_2 (high cut-off wavenumber). On using this filter, only spectral content relevant to the target ensemble can be admitted, without loss of information or unwanted side-effects (ripples, phase-shifts, Gibbs effects etc.).

The one-dimensional profiles (A.2), (A.3) and (A.6) – (A.6) can readily be expanded to two dimensions. At each position (k_x, k_y) of the Fourier plane, the modulus $|k| = \sqrt{k_x^2 + k_y^2}$ represents a radial wavenumber. Thus, if $|\mathbf{k}|$ is the matrix of radial wavenumbers, it is easy to generate a two-dimensional radial Meyer window scaled and localized with respect to some $|k_0|$, by letting $\mathbf{r} = |\mathbf{k}|/|k_0|$, with $|k_0|$ still determinable as before, on the basis of the radially averaged power spectrum ($k_0 \equiv |k_0|$). Likewise, it is possible to construct two-dimensional Radial EMW (REMW) filters. For instance, the band-pass REMW filter is

$$F(\mathbf{k}) = \begin{cases} \cos\left[\frac{\pi}{2} w(5 - 5\frac{\mathbf{k}}{k_1})\right], & \frac{2}{3} \le \frac{5}{6}\frac{\mathbf{k}}{k_1} \le \frac{5}{6} \\ 1, & k_1 < \mathbf{k} < k_2 \\ \cos\left[\frac{\pi}{2} w(3\frac{\mathbf{k}}{k_2} - 4)\right], & \frac{4}{3} \le \frac{4}{3}\frac{\mathbf{k}}{k_2} \le \frac{5}{3} \\ 0, & otherwise \end{cases}$$

with $k_1 \equiv |k_1|$ and $k_2 \equiv |k_2|$ again determinable through the radially averaged power spectrum.

A number of two-dimensional filters is illustrated in Fig A2. Specifically, Fig. A2a shows a radial Meyer window localized around k_0 = 0.3762cycles/km; it comprises the two-dimensional extension of the Meyer window depicted in Fig. A1a. Fig. A2b illustrates a band-pass REMW filter comprising the two-dimensional extension of the band-pass EMW shown in Fig. A1b; it is designed to exactly separate a depth-limited ensemble buried between Z_1 = 3.8km, (k_1 = 0.2592 cycles/km) and Z_2 = 1.8km (k_2= 0.5576 cycles/km). The differences in the pass band of the radial MW and EMW filters are rather apparent. In order to facilitate comparisons, as well as for the sake of completeness, Fig. A2c illustrates a two-dimensional extension of the corresponding band-pass Wiener filter based on the Blakely response (see Fig. A1a). Finally, Fig. A2d illustrates a low-pass REMW filter designed to suppress information from all depths greater than Z_2 = 1.8km ($|k_2|$= 0.5576 cycles/km). A high-pass REMW filter is an exact complement of the low-pass variant so that examples are not shown for brevity.

Table 1: All known crustal (D < 30km) focal mechanisms at the broader area of the Argolid. Data sources are as follows. RTS: Ritsema (1974); HATZ: Hatzfeld et al. (1993); CGMT: Global Centroid Moment Tensor Catalogue, http://www.globalcmt.org; KONST: Konstantinou et al., (2010); UoA: Laboratory of Seismology, University of Athens, http://dggsl.geol.uoa.gr; NOA: Institute of Geodynamics, National Observatory of Athens, http://bbnet.gein.noa.gr/HL; AUTH: Seismological Laboratory, University of Thessaloniki.

Year	Month	Day	h	min	Location (Source)			ISC Location			M_w	Strike	Dip	Rake	Source
					Lon	Lat	D	Lon	Lat	D					
1968	7	4	21	47	23.20	37.7	15	23.23	37.76	20	5.5	97	58	-65	RTS
1988	7	14	17	08	23.03	37.71	17	NA	NA	NA	2.0	49	70	1	HATZ
1988	7	14	20	40	23.01	37.70	13	NA	NA		2.0	250	49	89	HATZ
1988	8	17	12	08	23.11	37.72	17	NA	NA		2.5	205	30	-90	HATZ
1988	8	18	12	00	23.08	37.73	11	NA	NA		2.4	199	60	-90	HATZ
1999	9	7	11	56	23.64	37.87	15	23.582	38.122	9.4	5.9	116	39	-81	GCMT
2002	1	24	3	59	22.81	38.06	5	NA	NA	NA	3.5	67	80	-86	KONST
2002	9	7	20	22	22.85	37.10	13.0	22.975	37.172	17.8	3.8	76	84	-19	KONST
2002	11	23	1	14	22.56	37.98	12.0	22.642	38.031	22.1	3.8	62	66	-85	KONST
2004	2	17	15	56	22.63	38.07	5.0	22.657	38.108	20	3.9	127	37	-50	KONST
2006	9	10	4	40	22.70	38.10	5.0	22.769	38.099	14.4	4.0	98	24	-50	KONST
2006	11	16	18	50	23.10	36.96	8.0	23.231	36.960	10.5	3.6	67	26	-6	KONST
2008	1	29	15	16	23.517	37.643	8.0	23.437	37.604	13.4	4.2	109	52	-106	UoA
2008	4	14	12	25	23.2593	37.854	12.0	NA	NA	NA	3.4	85	48	-62	UoA
2008	8	3	13	01	23.4911	37.3948	10.0	23.486	37.332	9.1	3.9	118	70	-74	UoA
2008	9	18	07	02	23.7326	37.066	12.0	23.704	37.0398	9.7	3.8	120	65	-80	UoA
2008	9	30	0	43	23.2894	38.1139	8	NA	NA	NA	3.7	108	62	-90	UoA
2009	3	6	1	45	22.9296	37.5797	5.0	22.9302	37.6073	14.4	3.8	106	79	-102	UoA
2009	5	17	11	59	22.69	38.13	6.0	22.6944	38.1194	13.9	4.6	103	41	-89	AUTH
2009	9	2	9	35	23.32	38.11	5.0	23.2739	38.1082	9.4	4.0	106	34	-74	NOA
2010	12	14	13	58	22.83	38.08	16.0	22.7868	38.0608	13.7	3.9	133	84	-7	NOA
2011	1	31	17	23	22.70	37.87	17.0	22.7131	37.8784	16.3	3.5	160	60	-31	NOA
2011	10	24	9	24	23.509	37.609	9.0	23.5118	37.6070	12.9	3.5	118	31	-115	NOA
2011	12	08	20	59	23.5252	38.0838	7.0	23.5121	38.0980	10.5	3.6	113	53	-73	NOA
2012	2	17	8	5	23.044	37.865	14.0	23.0322	37.8503	11.4	4.1	126	45	-85	UoA
2012	9	22	3	52	22.7377	38.086	25.0	NA	NA	NA	4.9	102	70	-98	NOA
2012	12	4	18	59	23.100	36.9253	10.0	NA	NA	NA	4.3	171	46	-71	NOA
2012	12	5	3	27	23.0605	36.9232	8.0	NA	NA	NA	3.5	178	56	-60	NOA
2012	12	6	17	48	23.1094	36.9453	13.0	NA	NA	NA	4.4	171	51	-71	NOA
2012	12	9	1	23	22.5970	37.9278	12.0	NA	NA	NA	4.0	97	31	-95	UoA
2012	12	13	6	36	23.3267	37.5160	12.0	NA	NA	NA	3.4	77	79	-171	NOA
2013	6	4	1	56	23.9645	37.9612	21.0	NA	NA	NA	4.0	125	33	-83	NOA
2013	11	27	14	21	23.0101	37.3418	20.0	NA	NA	NA	4.3	144	88	-96	UoA
2014	4	10	17	40	22.6132	37.9257	10.0	NA	NA	NA	3.5	99	45	-91	NOA
2014	6	28	19	9	22.8515	37.4625	14.0	NA	NA	NA	3.7	86	81	-143	NOA
2014	9	14	22	41	23.0888	37.6978	13.0	NA	NA	NA	3.9	161	80	-111	NOA
2014	9	16	41	40	23.0037	37.1812	21.0	NA	NA	NA	3.9	183	77	-129	NOA
2014	9	18	24	25	23.0888	37.6978	13.0	NA	NA	NA	3.8	123	57	-106	NOA

Table 2: The strength and depth parameters of magnetic source ensembles, calculated on the basis of 5000 solutions to Eq. (1) obtained with the bootstrapping procedure described in the text. Results are given in the form of ensemble averages $\langle X \rangle$ and ensemble standard deviations ($\sigma_{\langle X \rangle}$).

Ensembles	**1**	**2**	**3**	**4**	**5**	$\boldsymbol{A_n}$
$\langle A_j \rangle \pm \sigma_{\langle Aj \rangle}$	63.36 ± 10.9	443.97 ± 43.29	28.03 ± 0.53	0.11 ± 0.03	$2\times10^{-4} \pm 1\times10^{-5}$	$1.6\times10^{-5} \pm 2\times10^{-6}$
$\langle Z_j \rangle \pm \sigma_{\langle Zj \rangle}$	6.8 ± 0.92	3.74 ± 0.09	1.8 ± 0.02	0.75 ± 0.004	0.3 ± 0.009	

FIGURE 1

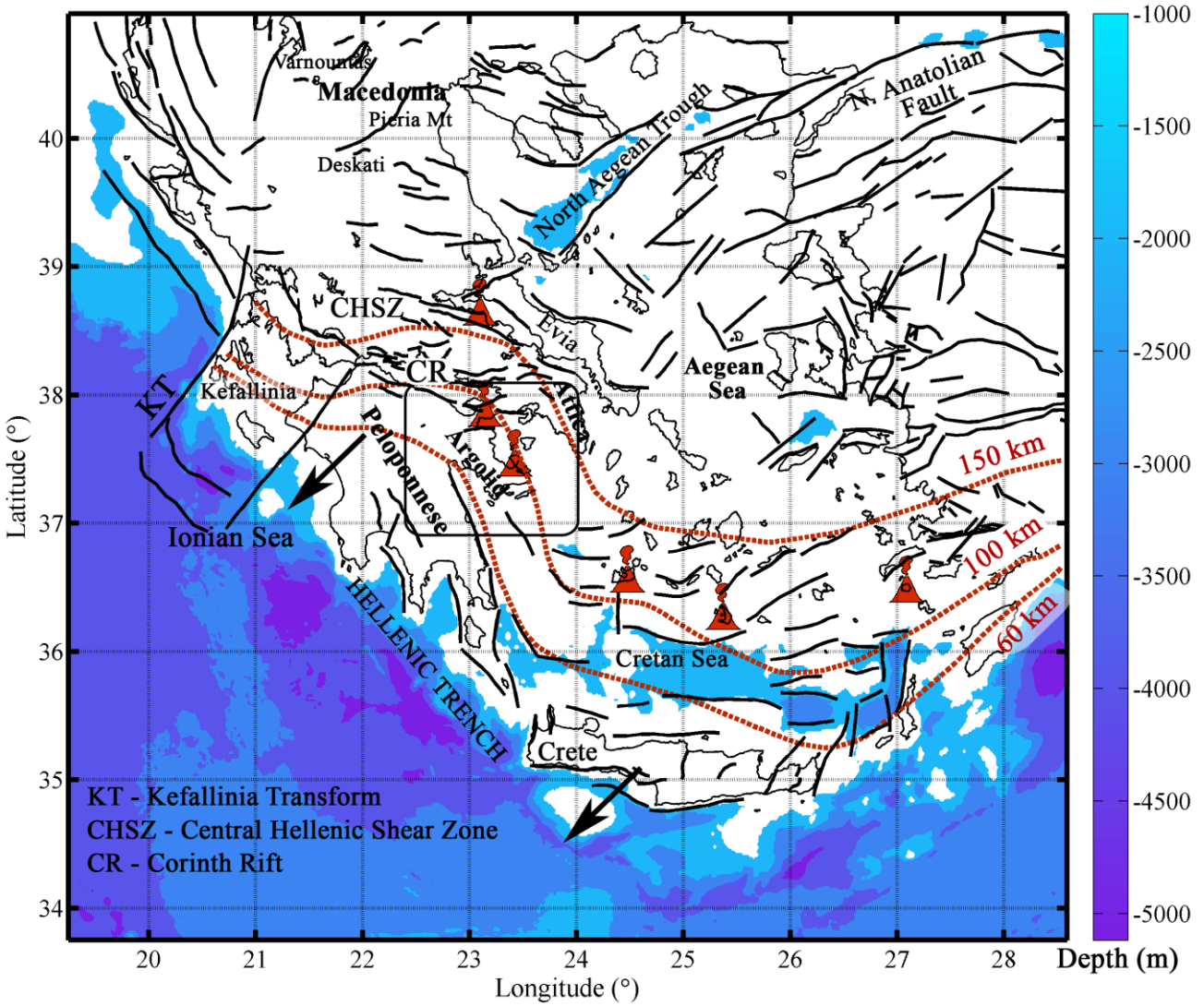

Figure 1: Synoptic depiction of the Hellenic Subduction System. The fields of the Hellenic Volcanic Arc are indicated with "smoking volcano" symbols. The study area is outlined by the rounded rectangle between latitudes 36.9°N – 38.1°N and longitudes 22.4°E – 24°E. The black arrows indicate the motion of the Aegean plate relative to the African. The thick red dashed lines indicate the 60, 100 and 150 kilometre iso-depths of the subducting slab and thick black solid lines indicate active faults; both data sets were extracted from the SHARE database (Basili et al., 2013). Bathymetry was extracted from the ETOPO1 database (Amante and Eakins, 2009).

FIGURE 2

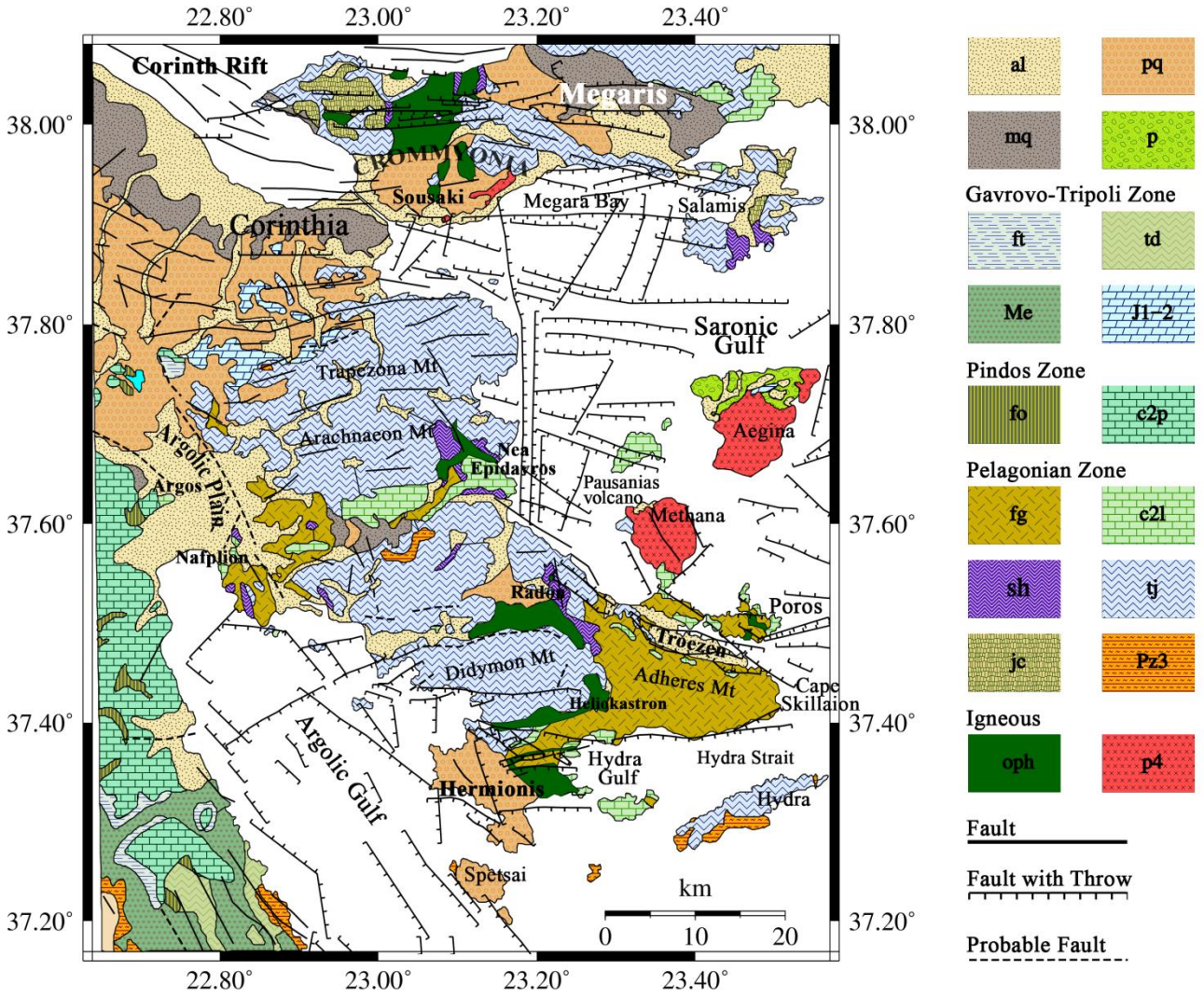

Figure 2: Geological and location map of the study area. Codenames of geological formations are as follows: *Cainozoic*: **al**, alluvial deposits; **pq**, Plio-Pleistocene lacustrine and marine sediments; **mq**, Pleistocene lacustrine and terrestrial sediments; **p**, Pliocene marine sediments. *Tripoli and Parnassus zone*: **ft**, flysch; **td**, Middle-Late Triassic dolomites; **Me**, Mesozoic–Eocene limestones and dolomites undivided; **J1-2**, Early-Middle Jurassic limestones. *Pindos zone*: **fo**, flysch; **c2p**, Late Cretaceous limestones. *Pelagonian zone*: **fg**, flysch; **c2l**, Late Cretaceous limestones; **sh**, shale-chert formation (ophiolitic-sedimentary mélange); **tj**, Triassic – Jurassic limestones (Didyma – Trapezona Formation); **jc**, Boeotian flysch; **Pz3**, various Late Palaeozoic and Permotriassic formations, unclassified. *Igneous*: **oph**, generic classification of ophiolitic rocks (generally harzburgites, serpentinites, gabbros, amphibolites, andesitic lavas in schistose serpentinine matrix); **p4**, generic classification of Quaternary calc-alkaline volcanic rocks (andesites to dacites). Fault data was collected from Papadeas (1989), Kokkalas and Aydin (2012), Skourtsos and Kranis (2009), Papanikolaou et al. (1988), Vassilopoulou (1999), Kranis (1999), Palyvos (2001) and Stefatos et al. (2002). The map was created with version 5.3 of the GMT software package (Wessel et al., 2013).

FIGURE 3

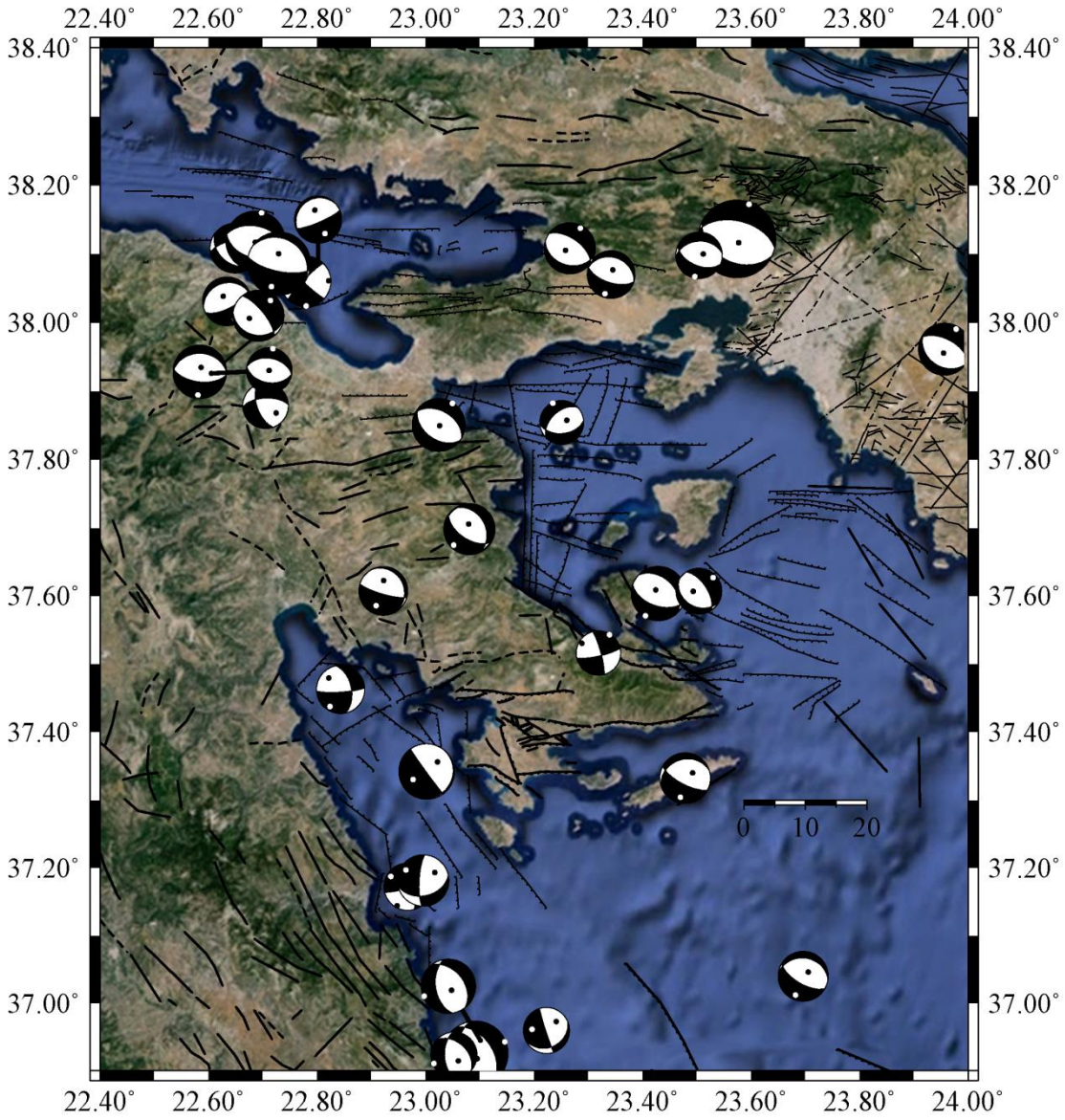

Figure 3: Fault traces and focal mechanisms of post-1990 crustal earthquakes in the broader area of the Argolid; the beach balls of pre-2012 mechanisms are plotted on their ISC primary coordinates; when available, see Table 1 for details. The map was created with version 5.3 of the GMT software package (Wessel et al., 2013).

FIGURE 4

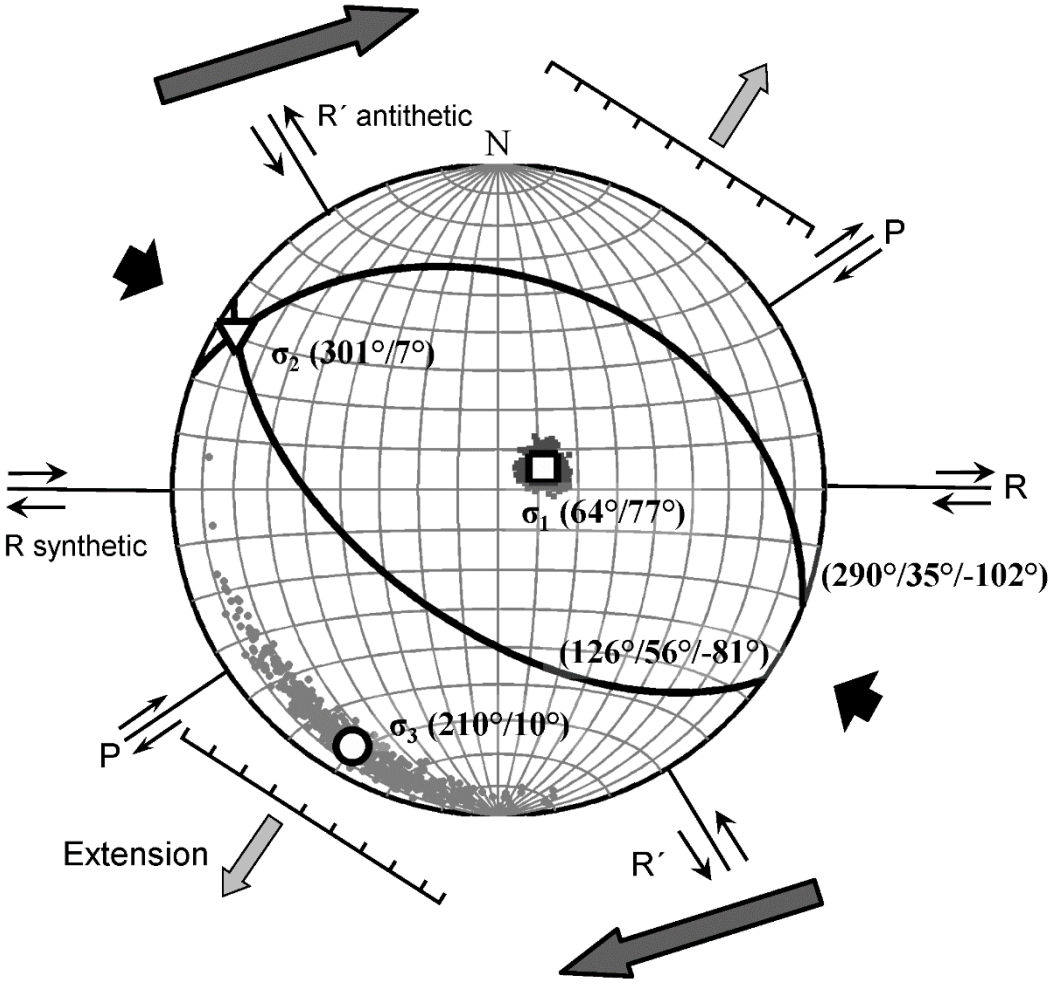

Figure 4: Schmidt projection of the stress field obtained by inversion of 22 post-2002 mechanisms with M_w between 3.8 and 4.9. Grey squares and circles indicate estimates produced by bootstrap resampling and the expanse of the 95% confidence area for σ_1 and σ_3 respectively. The "typical" expected faulting mechanisms and the schematics of the faulting pattern predicted by Riedel shear theory are also projected.

FIGURE 5

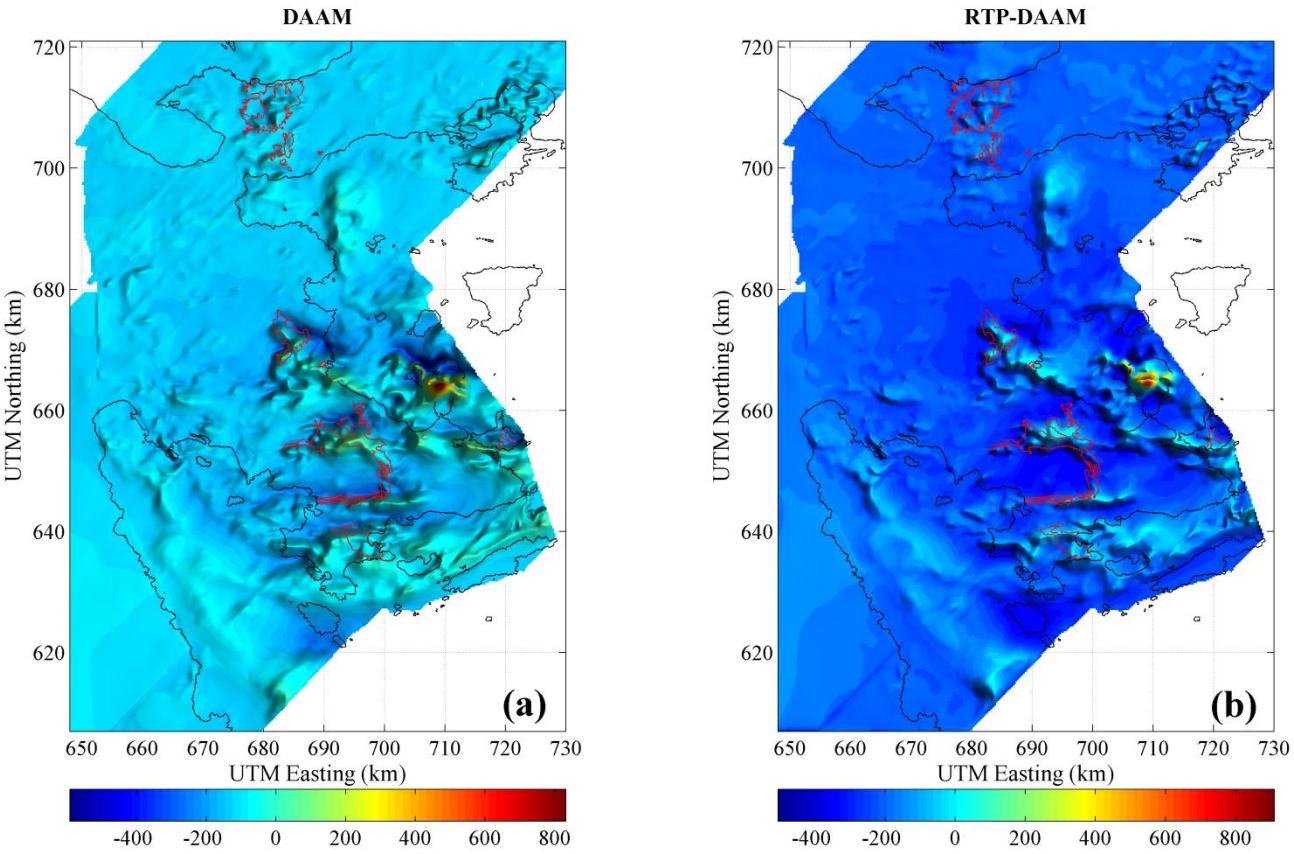

Figure 5: (a) The Digital Aeromagnetic Anomaly Map (DAAM) observed at a constant clearance of 300m AGL. **(b)** Reduced to the pole (RTP) version of the DAAM. Magnetic intensity units are given in nT. Both maps are shown in shaded relief mode to facilitate visualisation of small-amplitude and deep-seated anomalies. The outcrops of ophiolitic formations are also outlined. UTM northings were reduced by 3500 km so as to facilitate the display.

FIGURE 6

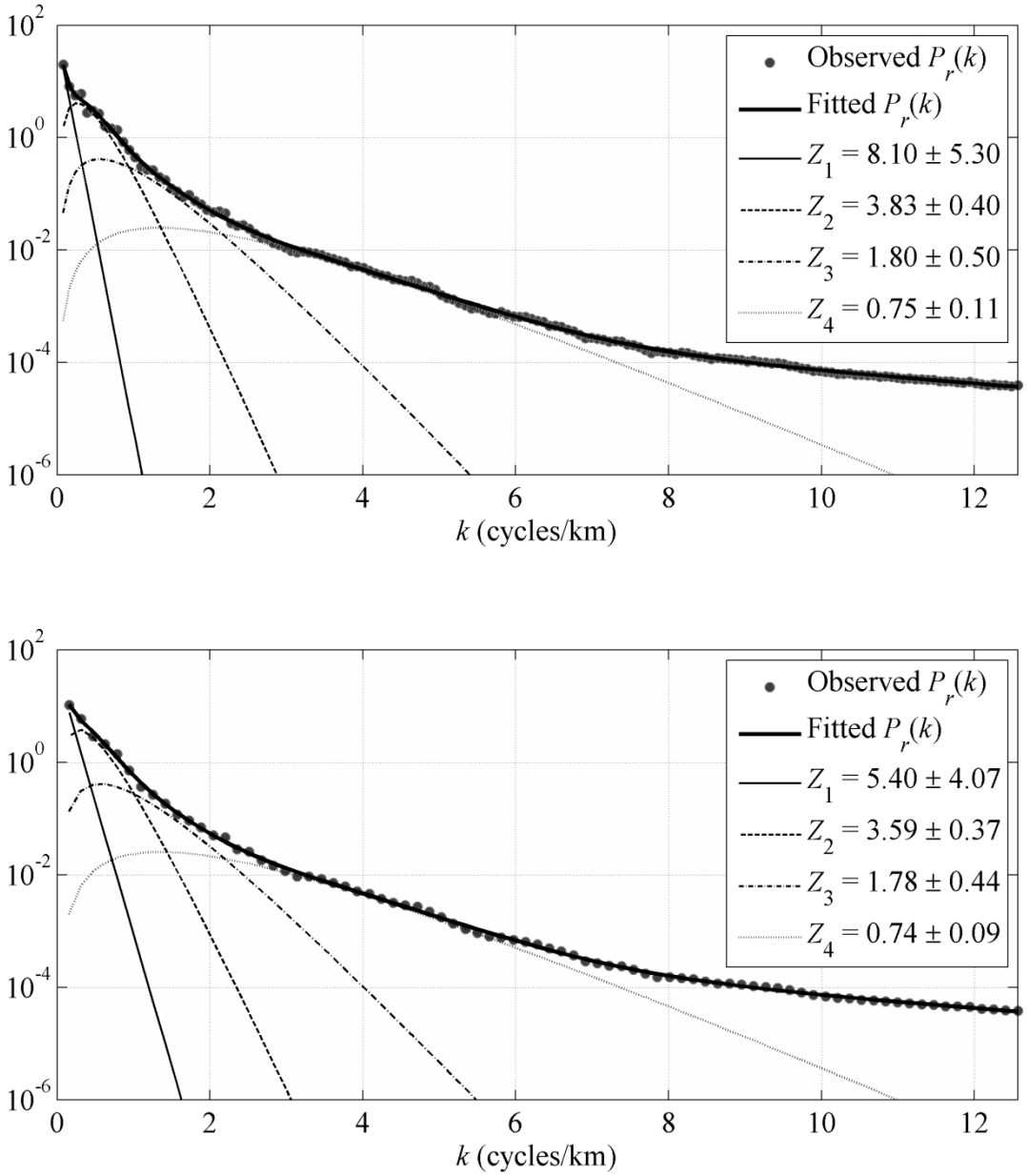

Figure 6: Modelling of two realizations of radially-averaged power spectral density derived from the RTP anomaly (Fig. 5b), using different radial partitioning schemes that yield different resolutions. In both panels, solid grey circles represent the observed radial spectra and thick solid black lines the best fitting models based on Eq. (1). The other thin lines represent the responses of individual magnetic source ensembles buried at the depths $Z_1 - Z_4$, as indicated in the legends.

FIGURE 7

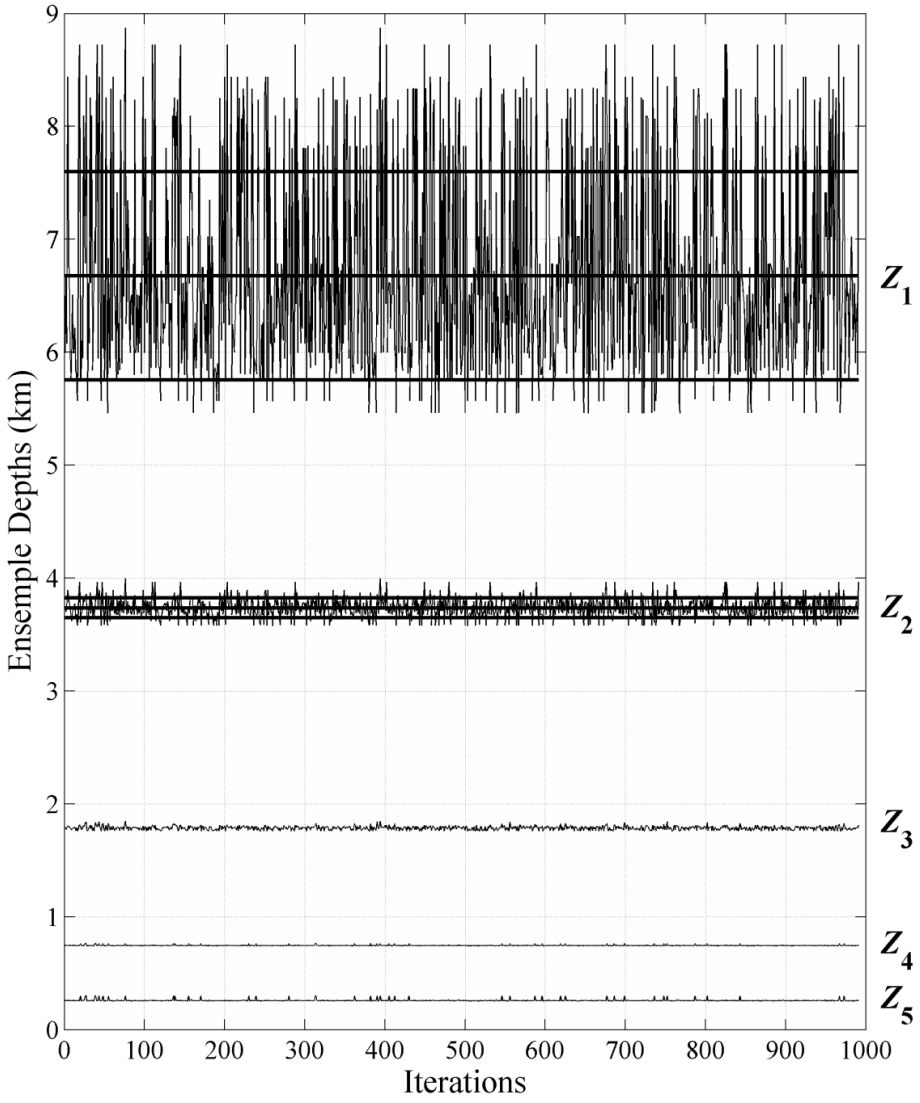

Figure 7: Estimation of the depth to the magnetic source ensembles based on Eq. (1) and 1000 random realizations of the radially averaged power spectrum (see text for details). The horizontal lines indicate the expectation values and 68% confidence limits of the two deeper ensembles (Z_1 and Z_2).

FIGURE 8

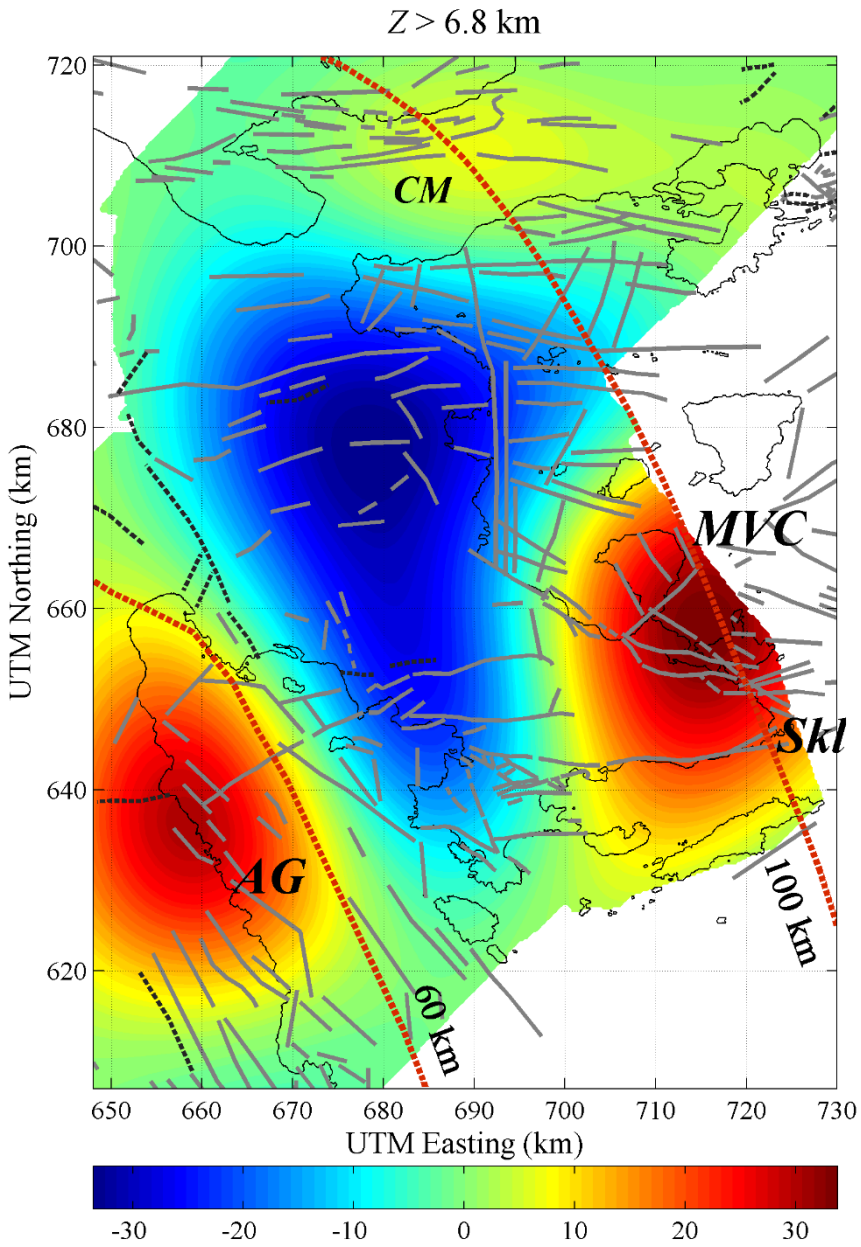

Figure 8. RTP magnetic anomalies generated by basal (depth-unlimited) sources, buried at depths greater than 7km below flight level (low-pass filtered). Magnetic intensity units are given in nT. The anomalies are geographically referenced: *AG*: Argolic Gulf; *Skl*: Cape Skillaion; *MVC*: Methana Volcanic Complex; *CM*: Crommyonia - Megaris. Broken lines indicate the location of the 60km and 100km isodepths to the top of the subducting slab (after Basili et al., 2013). UTM northings were reduced by 3500 km so as to facilitate the display.

FIGURE 9

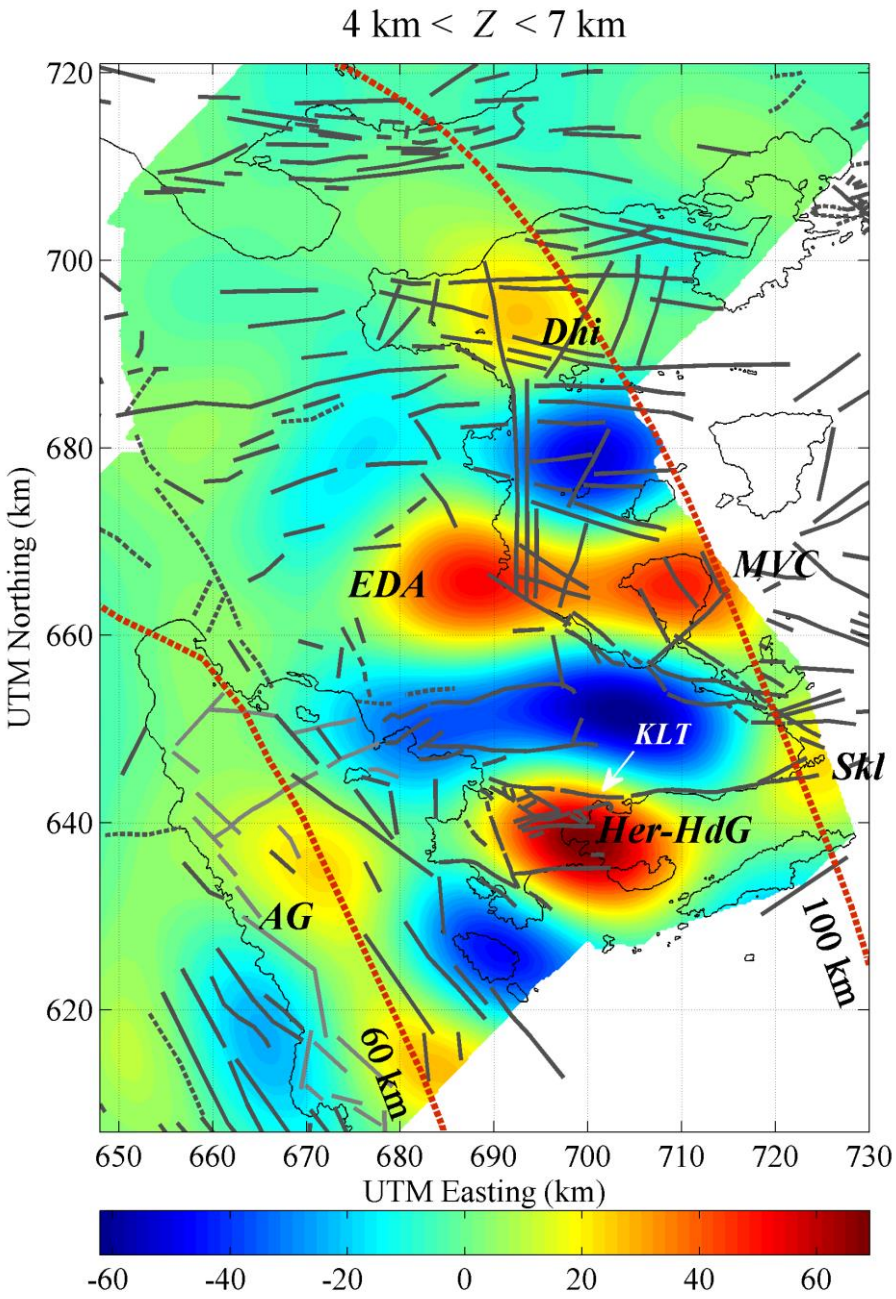

Figure 9: RTP magnetic anomalies generated by sources buried at depths between 7km and 4km below flight level (band-pass filtered). Magnetic intensity units are given in nT. The geographic references are: *AG*: Argolic Gulf; *Her-HdG*: Hermionis-Hydra Gulf anomaly; *Skl*: Cape Skillaion anomaly; *MVC*: Methana Volcanic Complex; *EDA*: Epidavros Deep Anomaly; *Dhi*: Dhiaporian Islets – Megara Gulf anomaly. *KLT* is the Koilada-Loutra-Thermisia fault zone. Broken lines indicate the location of the 60km and 100km isodepths to the top of the subducting slab (after Basili et al., 2013). UTM northings were reduced by 3500 km so as to facilitate the display.

FIGURE 10

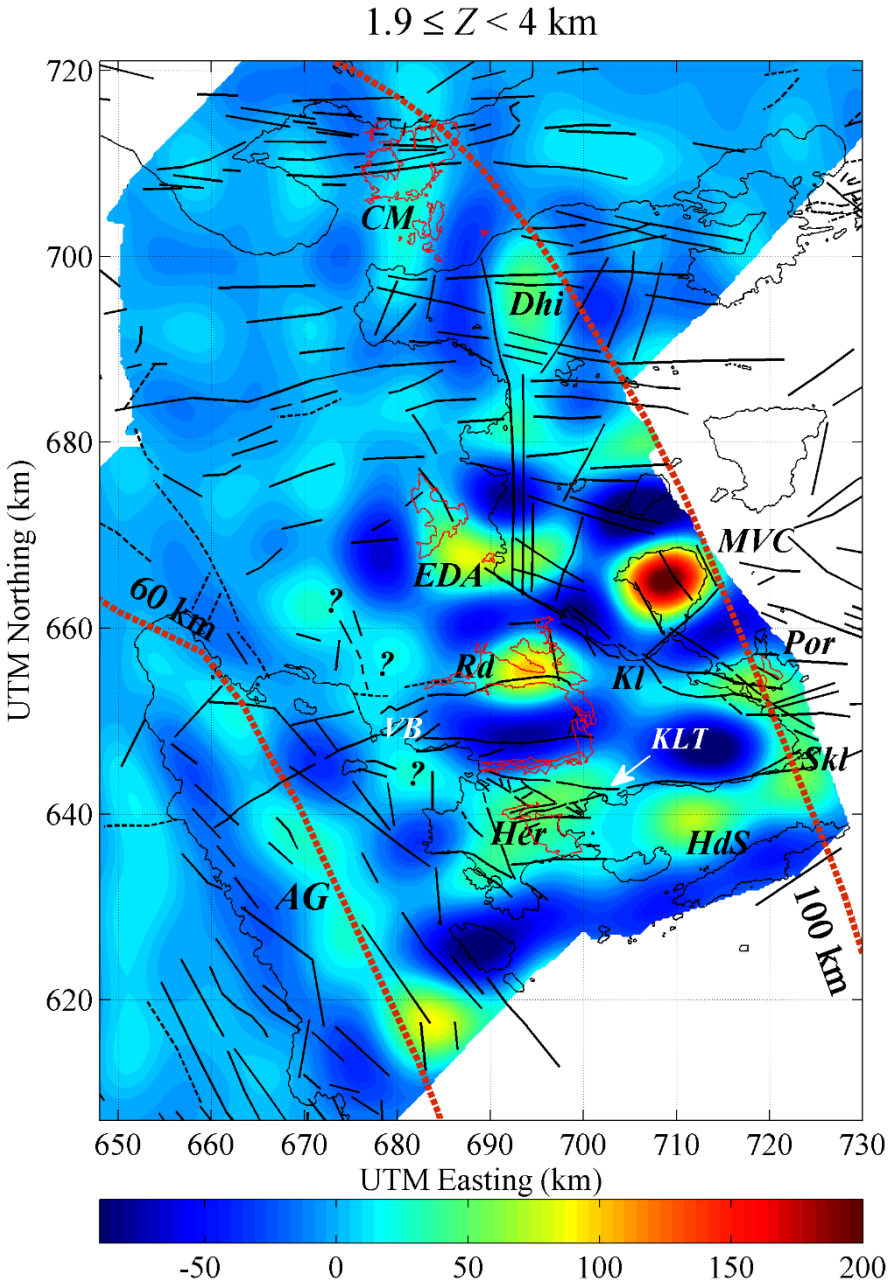

Figure 10: RTP magnetic anomalies generated by sources buried at depths between 2km and 4km below flight level. Magnetic intensity units are given in nT. The geographic references are: *AG*: Argolic Gulf; *Her*: Hermionis anomaly; *HdS*: Hydra Strait anomaly; *Skl*: Cape Skillaion anomaly; *Por*: Poros anomaly; *MVC*: Methana Volcanic Complex; *EDA*: Epidavros Deep anomaly; *Rd*: Radon anomaly; *Kl*: Kalloni; *Dhi*: Dhiaporian Islets – Megara Gulf anomaly; *CM*: Crommyonian anomaly. *VB* marks the location of Vourlos Bay; *KLT* is the Koilada-Loutra-Thermisia fault zone. Broken lines indicate the location of the 60km and 100km isodepths to the top of the subducting slab (after Basili et al., 2013). UTM northings were reduced by 3500 km so as to facilitate the display.

FIGURE 11

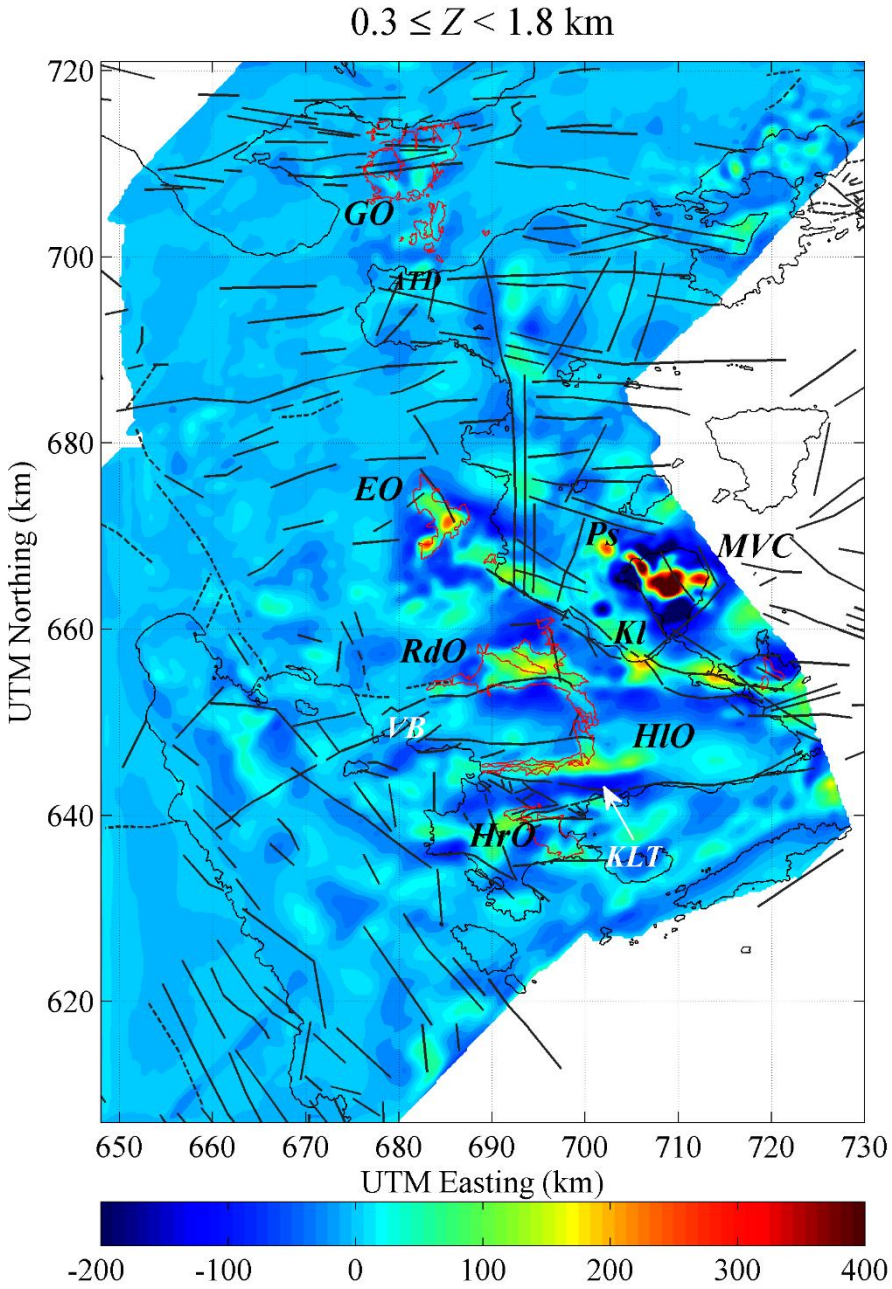

Figure 11: RTP magnetic anomalies generated by sources buried between 2km and 0.3km below flight level. Magnetic intensity units are given in nT. The geographic references are: *HlO*: Heliokastron Ophiolites; *HrO*: Hermioni Ophiolites; *RdO*: Radon Ophiolites; *Kl*: Kalloni anomaly; *MVC*: Methana Volcanic Complex; *Ps*: Pausanias submarine volcano; *EO*: Epidavros Ophiolites; *ATD*: Aghioi Theodoroi Dacite; *GO*: Gerania Ophiolites. *VB* marks the location of Vourlos Bay; *KLT* is the Koilada-Loutra-Thermisia fault zone. The outcrops of *HlO, HrO, RdO, EO* and *GO* are also outlined in red. UTM northings were reduced by 3500 km so as to facilitate the display.

FIGURE 12

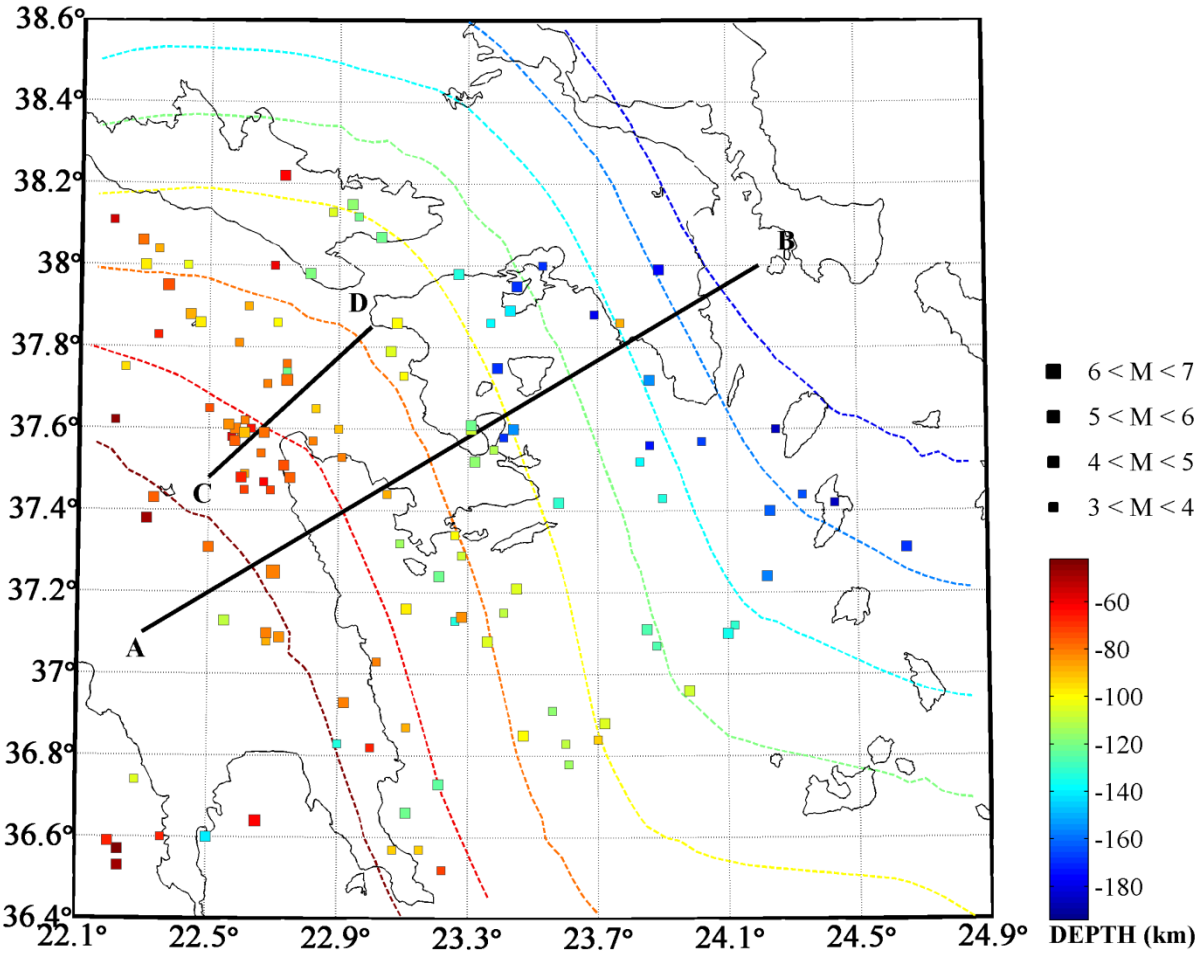

Figure 12: The hypocentral distribution of sub-crustal (> 40km) earthquakes observed in the broader study area over the period 1965–2012. Earthquake data has been extracted from the on-line bulletin of the International Seismological Centre (http://www.isc.ac.uk). Only earthquakes with $m_b \geq 3.5$ magnitudes are shown. AB marks the geographical location of the cross-section shown in Fig. 13 T. CD marks the location of the magnetotelluric cross-section shown in Fig. 13. The broken lines represent are isodepths of the ceiling of the subducting slab and have been extracted from the SHARE database (Basili et al., 2013).

FIGURE 13

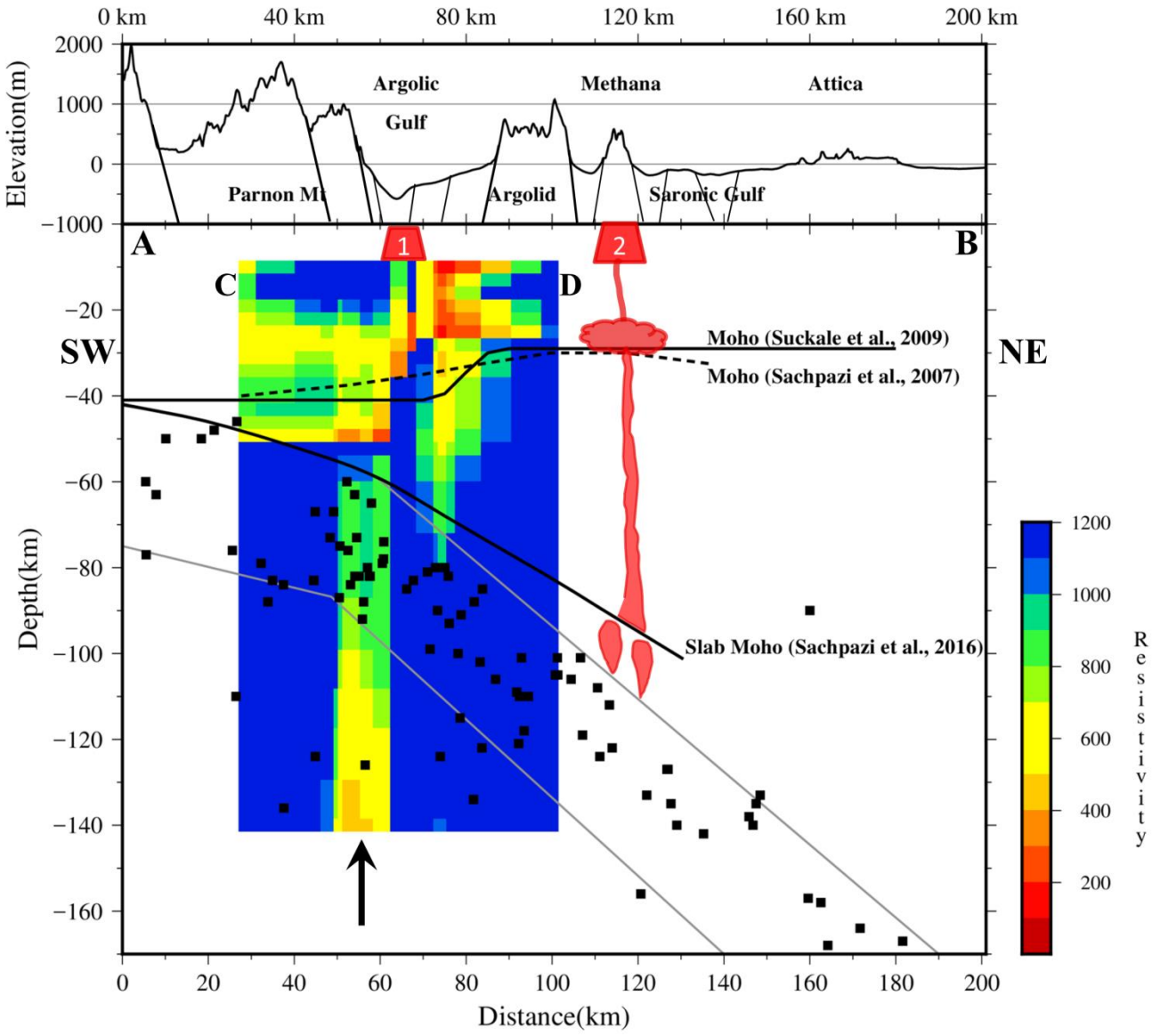

Figure 13: Composite cross-section along the profile AB of Fig. 12. The bottom panel illustrates: a) The projection of the sub-crustal earthquake hypocentres of Fig. 12 on the profile AB. b) The electrical resistivity cross-section along the profile CD of Fig. 12, rotated parallel to AB plane and projected on the AB plane. c) A profile of the Mohorovičić discontinuity of the Aegean plate according to Sachpazi et al., (2007), collocated with profile AB. d) A profile of the Mohorovičić discontinuity of the Aegean plate according to Suckale et al., (2009), rotated to the orientation of AB and projected on the AB plane. e) A profile of the ceiling of the subducting slab taken from the tomographic image shown in Fig.1 of Sachpazi et al., (2016), which is approximately collocated with the CD plane, rotated to the orientation of AB and projected on the AB plane. The top panel is a vertically exaggerated topographic section along AB, drawn together with major normal faults. The red trapezoids indicate the large magnetic sources detected along the axis of the Argolic Gulf (1) and at the Methana Volcanic Complex (2).

FIGURE 14

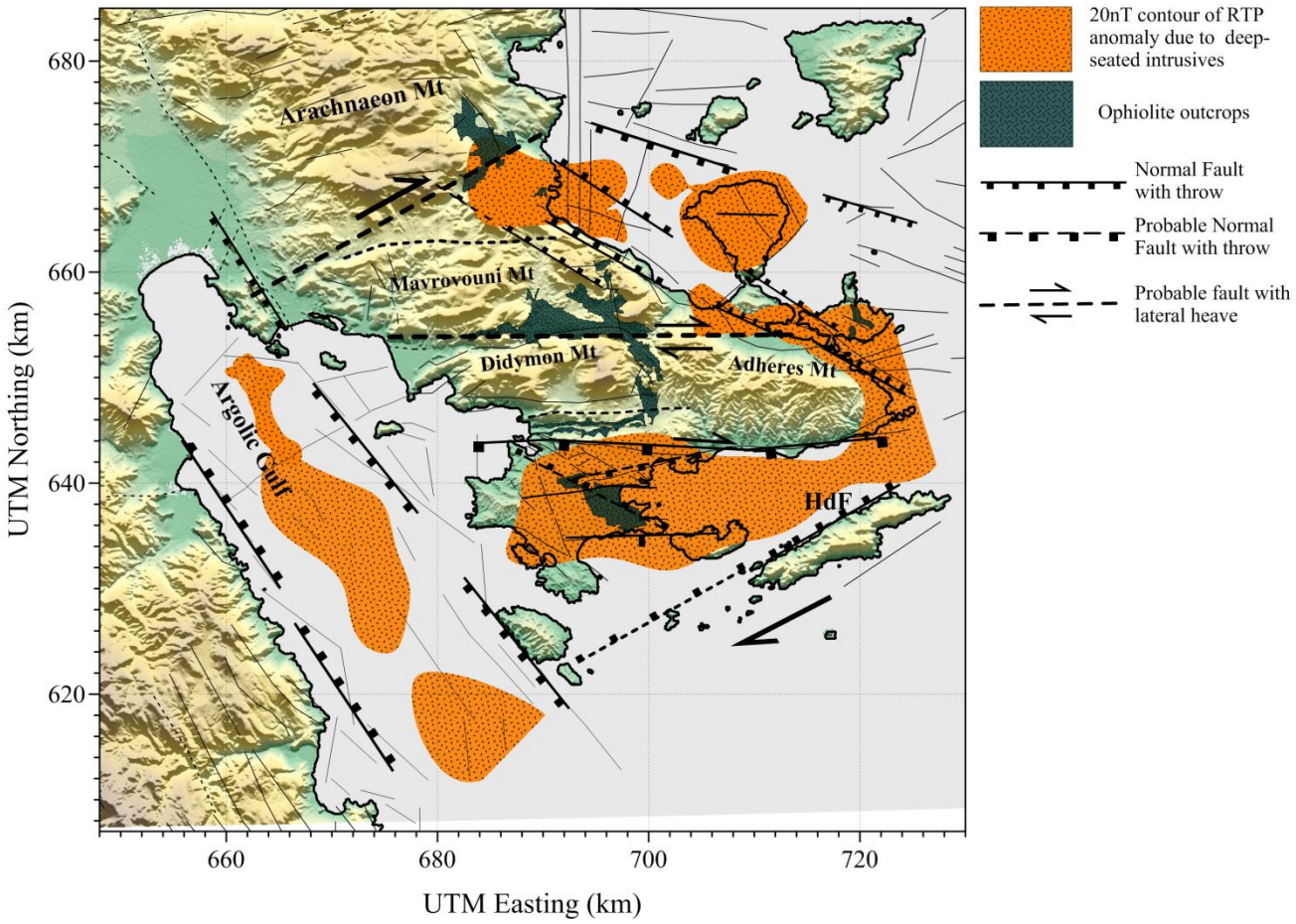

Figure 14: Tentative tectonic model for the area of Argolis peninsula. UTM northings were reduced by 3500 km so as to facilitate the display.

FIGURE A1

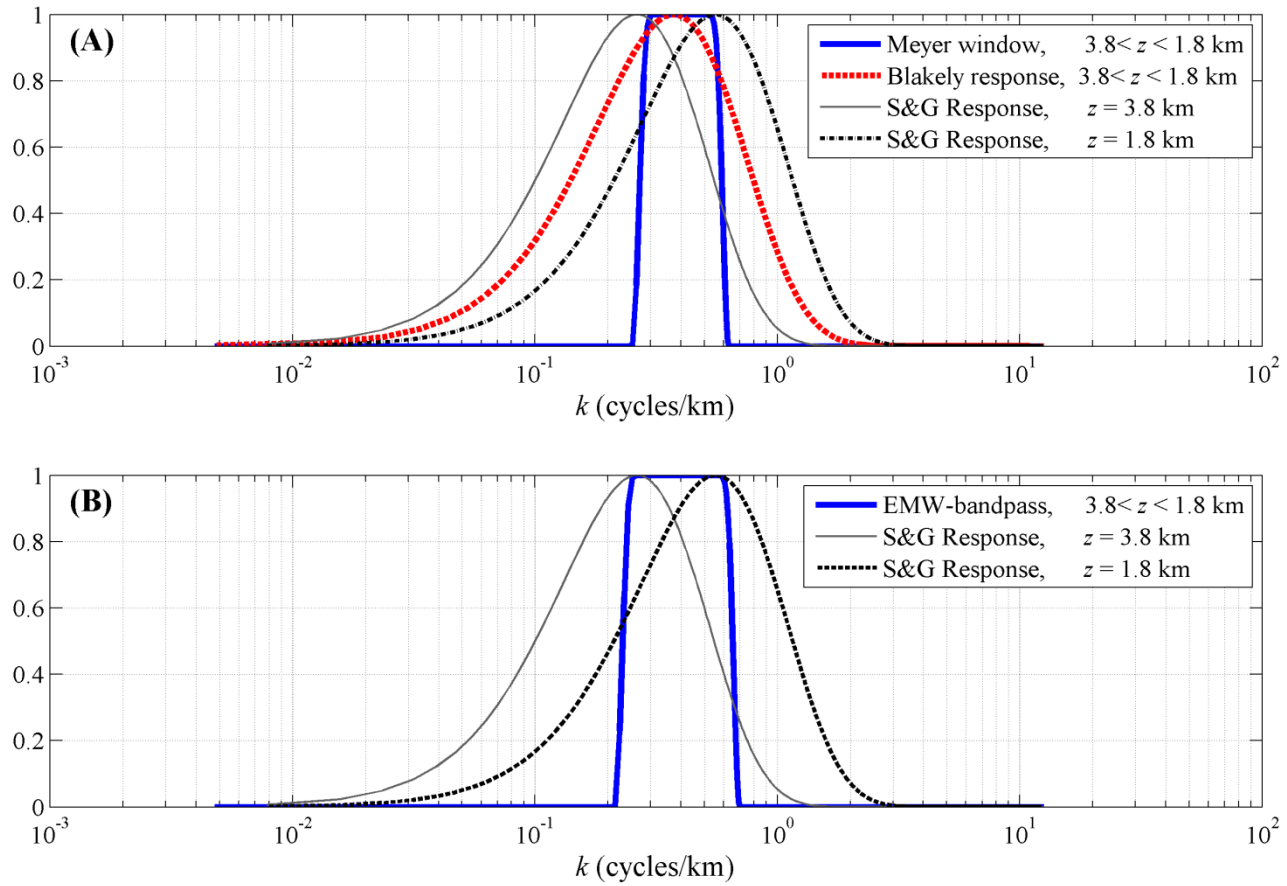

Figure A1: Different band-pass filters intended to isolate a magnetic source ensemble buried between 3.8 and 1.8 km. **(A)** Comparison of Wiener filters based on the Spector and Grant (S&G) and Blakely responses, to a Meyer Window filter localized (tuned) with respect to the peak of the Blakely response. **(B)** Realization of an Extended Meyer Window filter localized with respect to the peaks of the S&G responses for Z_1 = 3.8 and Z_2 = 1.8 km (see text for details).

FIGURE A2

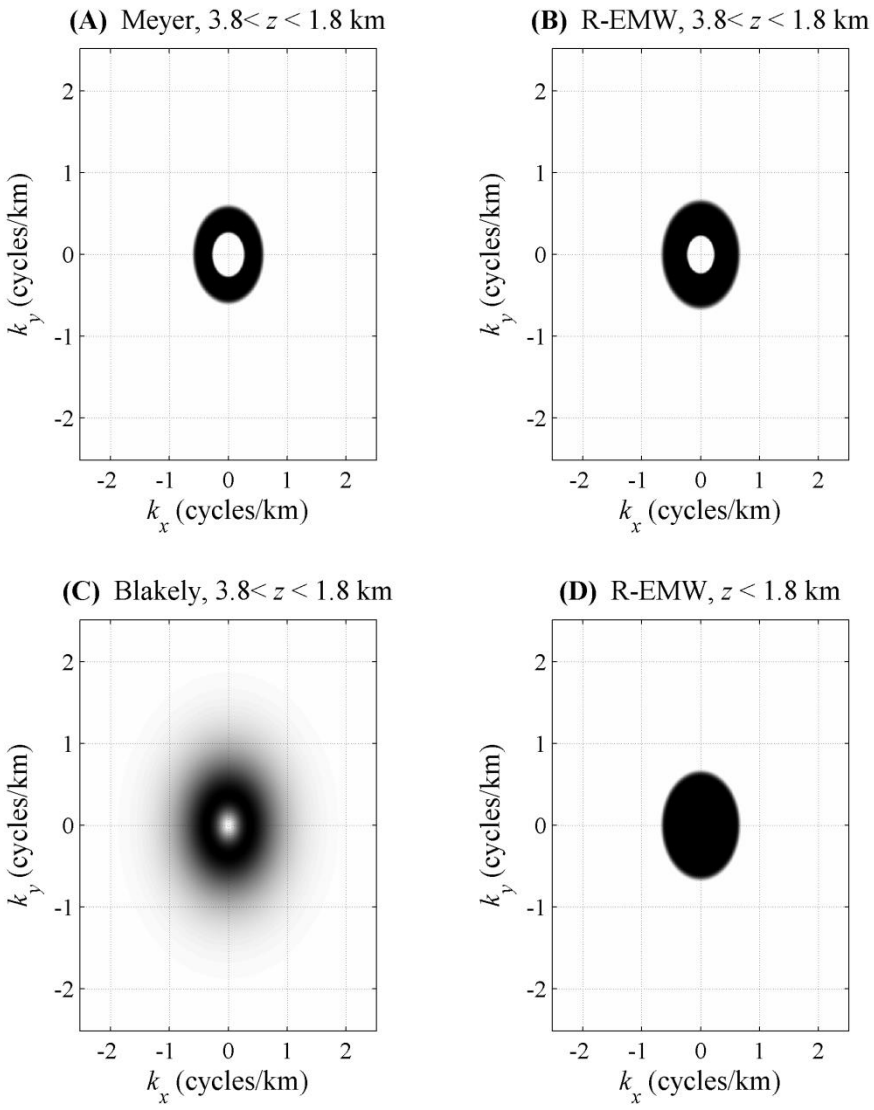

Figure A2: Two-dimensional band-pass and low-pass filters intended to isolate magnetic anomalies generated by magnetic sources buried between Z_1 = 3.8km and Z_2 = 1.8km. **(a)** Band-pass Radial Meyer Window comprising 2-D extension of the Meyer Window profile shown in Fig. A1a. **(b)** Band-pass Radial Extended Meyer Window comprising D extension of the band-pass EMW shown in Fig. A1b. **(c)** Band-pass Wiener filter based on the Blakely response, 2-D extension of the Blakely response shown in Fig. A1a. **(d)** Low-pass Radial Extended Meyer Window with cutoff at $|k_2|$= 0.5576, designed to isolate sources buried at depths greater than Z_2.